J|A|C|S
ARTICLES

Morphology Phase Diagram of Ultrathin Anatase TiO_2 Films Templated by a Single PS-*b*-PEO Block Copolymer

Ya-Jun Cheng[†] and Jochen S. Gutmann,[*,†,‡]

Contribution from the Max-Planck Institute for Polymer Research, Ackermannweg 10, D-55128, Mainz, Germany, and Institute of Physical Chemistry, University of Mainz, Welderweg 11, D-55099, Mainz, Germany

Received September 12, 2005; E-mail: gutmann@mpip-mainz.mpg.de

Abstract: Ultrathin TiO_2 films showing rich morphologies are prepared on Si(100) substrates using sol−gel chemistry coupled with an amphilic polystyrene-*block*-poly(ethylene oxide) (PS-*b*-PEO) diblock copolymer as a structure-directing agent. The block copolymer undergoes a good−poor solvent pair induced phase separation in a mixed solution of 1,4-dioxane, concentrated hydrochloric acid (HCl), and titanium tetraisopropoxide (TTIP). By adjusting the weight fractions of 1,4-dioxane, HCl, and TTIP, inorganic block copolymer composite films containing a variety of different morphologies are obtained. On the basis of the results a ternary phase diagram of the morphologies is mapped. By calcination, anatase TiO_2 films are achieved. The morphologies and crystallographic phase of the films are studied with AFM, SEM, and XRD, respectively, and the formation mechanisms of the different morphologies are discussed.

Introduction

Synthesis of nanostructured TiO_2 thin films has attracted considerable interest in the past decade due to their intriguing physical properties and promising applications in photocatalysis, photovoltaics, gas sensing, and Li ion battery materials.[1−11] In many cases, the performance of these materials significantly depends on the morphology and crystallinity of the nanostructured TiO_2.[12−14] The morphology of the TiO_2 films controls the surface-to-volume ratio, which determines the active-site density on the surface available for surface reactions and interfacial charge carrier transfer rate. Furthermore, in photovoltaic materials different morphologies can provide varied charge carrier delocalization routes and as a result influence electron−hole pair recombination probabilities.[15−18] It is therefore very important to prepare TiO_2 thin films with reproducible morphologies. Besides morphology, crystallinity also plays an important role in titania-related materials because it determines the electronic structure of TiO_2. TiO_2 has three different crystallographic polymorphs, anatase, rutile, and brookite.[19] In many of the functional materials, anatase makes the most important contributions to the performance because of its thermodynamically metastable characteristics and preferred formation in nanoscale systems.[20−23] In comparison to anatase, rutile is more thermodynamically stable and chemically inert and brookite commonly does not form a pure crystallographic phase and in many cases coexists with anatase and/or rutile as a labile, metastable state.[24−26] Finally, the overall macroscopic size of the homogeneous structured titania films is another important requirement for their use in device applications. For example, in dye-sensitized solar cell (DSSC) devices, the films should fulfill the prerequisite to cover substrates of at least square millimeters.[27] To summarize, for the purpose of applications of titania thin films, it is crucial to prepare titania films

---

[†] Max-Planck Institute for Polymer Research.

[‡] University of Mainz.

(1) Linsebigler, A. L.; Lu, G. Q.; Yates, J. T. *Chem. Rev.* **1995**, *95*, 735−758.
(2) Heller, A. *Acc. Chem. Res.* **1995**, *28*, 503−508.
(3) Henderson, M. A. *J. Phys. Chem. B* **2005**, *109*, 12062−12070.
(4) Fujishima, A.; Zhang, X. T. *Proc. Jpn. Acad., Ser. B* **2005**, *81*, 33−42.
(5) Grätzel, M. *J. Photochem. Photobiol., A* **2004**, *164*, 3−14.
(6) Coakley, K. M.; McGehee, M. D. *Chem. Mater.* **2004**, *16*, 4533−4542.
(7) Figueroa, O. L.; Lee, C. H.; Akbar, S. A.; Szabo, N. F.; Trimboli, J. A.; Dutta, P. K.; Sawaki, N.; Soliman, A. A.; Verweij, H. *Sens. Actuators, B* **2005**, *107*, 839−848.
(8) Vargheses, O. K.; Grimes, C. A. *J. Nanosci. Nanotechnol.* **2003**, *3*, 277−293.
(9) Zuzuri, A. S.; MacDonald, N. C. *Adv. Funct. Mater.* **2005**, *15*, 396−402.
(10) Armstrong, A. R.; Armstrong, G.; Canales, J.; Garcia, R.; Bruce, P. G. *Adv. Mater.* **2005**, *17*, 862−865.
(11) Armstrong, G.; Armstrong, A. R.; Canales, J.; Bruce, P. G. *Chem. Commun.* **2005**, *19*, 2454−2456.
(12) Wang, Z. S.; Kawauchi, H.; Kashima, T.; Arakawa, H. *Coord. Chem. Rev.* **2004**, *248*, 1381−1389.
(13) Roberson, L. B.; Poggi, L. A.; Kowalik, J.; Smestand, G. P.; Bottomley, L. A.; Tolbert, L. M. *Coord. Chem. Rev.* **2004**, *248*, 1491−1499.
(14) Yan, M. C.; Chen, F.; Zhang, J. L.; Anpo, M. *J. Phys. Chem. B* **2005**, *109*, 8673−8678.
(15) Cozolli, P. D.; Kornowski, A.; Weller, H. *J. Am. Chem. Soc.* **2003**, *125*, 14539−14548.
(16) Baxter, J. B.; Aydil, E. S. *Appl. Phys. Lett.* **2005**, *86*, 053114.
(17) Law, M.; Greene, L. E.; Johnson, J. C.; Saykally, R.; Yang, P. D. *Nat. Mater.* **2005**, *4*, 455−459.
(18) Cass, M. J.; Walker, A. B.; Martinez, D.; Peter, L. M. *J. Phys. Chem. B* **2005**, *109*, 5100−5107.
(19) Wells, A. F. *Structural Inorganic Chemistry*; Clarendon Press: Oxford, 1975.
(20) Nagaveni, K.; Sivalingam, G.; Hegde, M. S.; Madras, G. *Appl. Catal., B* **2004**, *48*, 83−93.
(21) Zhang, H. Z.; Banfield, J. F. *J. Mater. Chem.* **1998**, *8*, 2073−2076.
(22) Zhang, H. Z.; Banfield, J. F. *J. Phys. Chem. B* **2000**, *104*, 3481−3487.
(23) d'Hennezel, O.; Ollis, D. E. *Helv. Chim. Acta* **2001**, *84*, 3511−3518.
(24) Yin, H.; Wada, Y.; Kitamura, T.; Kambe, S.; Murasawa, S.; Mori, H.; Sakata, T.; Yanagida, S. *J. Mater. Chem.* **2001**, *11*, 1694−1703.
(25) Hosono, E.; Fujihara, S.; Kakiuchi, K.; Imai, H. *J. Am. Chem. Soc.* **2004**, *126*, 7790−7791.
(26) Luo, H. M.; Wang, C.; Yan, Y. S. *Chem. Mater.* **2003**, *15*, 3841−3846.
(27) Peng, B.; Jungmann, G.; Jäger, C.; Haarer, D.; Schmidt, H. W.; Thelakkat, M. *Coord. Chem. Rev.* **2004**, *248*, 1479−1489.

10.1021/ja0562853 CCC: $33.50

with the desired morphology of the anatase phase on a mm^2 scale in a controllable and reproducible way.

There have been numerous reports about the synthesis of nanoscale titania materials with varied morphologies including nanoparticles, nanorods, mesoscale network structures, nanotubes, and lamellae.[11,15,28−36] The main preparation recipes apply titanium inorganic salts or titanium alkoxides as titanium sources, which are hydrolyzed and condensed to form Ti−O− networks in the presence of small molecule surfactants or block copolymers as structure-directing agents.[15,26,31,32,34−41] The Pluronic family of PEO−PPO−PEO triblock copolymers has been widely used as a template.[26,31,32,34,42−45] However, compared to the Pluronic copolymers, other kinds of block copolymers have been mainly used to template non-titania systems,[46−49] and until recently only a limited number of results about templating titania nanostructures have been reported.[50−57] For example, Smarsly et al. have used PHB-*b*-PEO ($H(CH_2CH_2CH_2CH(CH_3)-CH_3)_{66}(OCH_2CH_2)_{86}H$) diblock copolymer as the structure-directing agent to prepare crystalline titania mesoporous structures.[50] Wang et al. have applied PS-*b*-PEO as the template and obtained foamlike bicontinuous titania nanostructures.[57] Our group recently also reported the results using PS-*b*-PEO as a template to synthesize nanocomposite films composed of ordered titania nanoparticles.[52,53] Toluene and 2-propanol were used as the solvents, in which the block copolymer could undergo microphase separation to form micelles in the solution, and the titanium sol−gel precursor was subsequently incorporated into the micelles. After spin coating, composite films consisting of ordered nanoparticles were achieved.

With respect to the structure formation process, Eisenberg and co-workers have intensively studied the self-assembly behavior of amphilic block copolymer PS-*b*-PAA or PS-*b*-PEO in solution, where PAA and PEO are the minority parts of the block copolymer.[58−62] The block copolymers are dissolved into 1,4-dioxane, or DMF, which is a good solvent for both blocks, followed by slow addition of water, a selectively poor solvent for the PS block. As a result of the slow addition so-called crew-cut micelles with large PS cores and thin PEO or PAA coronas are formed in solution. The morphologies of the crew-cut micelles are controlled by a force balance between different factors: the stretching degree of the core-forming block, the interfacial force between the core and surrounding solvents, and interactions between the coronas. Eisenberg and co-workers have adjusted the solution components to tune the force balance and obtained rich morphologies such as spherical micelles,[62−64] cylinder micelles,[64−66] lamellae,[67,68] and vesicles.[69,70] However, the structures consist of only a pure organic polymer and lack a functional inorganic part. Furthermore, the obtained structures are present in solution, whereas in many applications the structures are required to be present in the form of dry films.

In this paper we are aiming to achieve the preparation of TiO_2 thin films with variable morphologies in a reproducible way through a simple recipe. A single amphilic diblock copolymer of PS-*b*-PEO is used as a structure-directing agent, and a so-called "good−poor solvent pair" induced phase separation process is coupled with sol−gel chemistry (Scheme 1).

The PS-*b*-PEO block copolymer with a PEO minor constitution part is first dissolved in 1,4-dioxane, which is a good solvent for both blocks, followed by successive addition of 37% concentrated HCl solution and titanium tetraisopropoxide (TTIP) within 3 min. The concentrated HCl solution is a poor solvent for the PS block; therefore, the interfacial energy between the PS block and solvents is increased leading to the formation of micelles in solution. The shape and size of the micelles in the solution are determined by the interfacial interactions between the PS block domain and the solvents surrounding the PS domain, the interactions between neighboring PEO domains, and finally the degree of stretching within the PS domains.[61,62] In addition to the HCl solution, the TTIP component in the solution will also influence the morphologies of the micelles

---

(28) Li, G. S.; Li, L. P.; Boerio-Goates, J.; Woodfield, B. F. *J. Am. Chem. Soc.* **2005**, *127*, 8659−8666.
(29) Gao, X. P.; Zhu, H. Y.; Pan, G. L.; Ye, S. H.; Lan, Y.; Wu, F.; Song, D. Y. *J. Phys. Chem. B* **2004**, *108*, 2868−2872.
(30) Mor, G. K.; Shankar, K.; Paulose, M.; Varghese, O. K.; Grimes, C. A. *Nano Lett.* **2005**, *5*, 191−195.
(31) Choi, S. Y.; Mamak, M.; Speakman, S.; Chopra, N.; Ozin, G. A. *Small* **2005**, *1*, 226−232.
(32) Yang, P. D.; Zhao, D. Y.; Margolese, D. I.; Chmelka, B. F.; Stucky, G. D. *Nature* **1998**, *396*, 152−155.
(33) Cho, Y. H.; Cho, G. J.; Lee, J. S. *Adv. Mater.* **2004**, *16*, 1814−1817.
(34) Crepaldi, E. L.; Soler-Illia, G. J. de A. A.; Grosso, D.; Cagnol, F.; Ribot, F.; Sanchez, C. *J. Am. Chem. Soc.* **2003**, *125*, 9770−9786.
(35) Alberius, P. C. A.; Frindell, K. L.; Hayward, R. C.; Kramer, E. J.; Stucky, G. D.; Chmelka, B. F. *Chem. Mater.* **2002**, *14*, 3284−3294.
(36) Carn, F.; Colin, A.; Achard, M. F.; Deleuze, H.; Sanchez, C.; Backov, R. *Adv. Mater.* **2005**, *17*, 62−66.
(37) Bai, N.; Li, S. G.; Chen, H. Y.; Pang, W. Q. *J. Mater. Chem.* **2001**, *11*, 3099−3102.
(38) Stathatos, E.; Lianos, P.; Monte, F. D.; Levy, D.; Tsiourvas, D. *Langmuir* **1997**, *13*, 4295−4300.
(39) Lin, J.; Lin, Y.; Liu, P.; Meziani, M. J.; Allard, L. F.; Sun, Y. P. *J. Am. Chem. Soc.* **2002**, *124*, 11514−11518.
(40) Anderson, M.; Osterlund, L.; Ljungstrom, S.; Palmqvist, A. *J. Phys. Chem. B* **2002**, *106*, 10674−19679.
(41) Wu, M. M.; Long, J. B.; Huang, A. H.; Luo, Y. J. *Langmuir* **1999**, *15*, 8822−8825.
(42) Angelome, P. C.; Aldabe-Bilmes, S.; Calvo, M. E.; Crepaldi, E. L.; Grosso, D.; Sanchez, C.; Soler-Illia, G. J. A. A. *New J. Chem.* **2005**, *29*, 59−63.
(43) Bartl, M. H.; Boettcher, S. W.; Frindell, K. L.; Stucky, G. D. *Acc. Chem. Res.* **2005**, *38*, 263−271.
(44) Wang, K. X.; Morris, M. A.; Holmes, J. D. *Chem. Mater.* **2005**, *17*, 1269−1271.
(45) Yu, J.; Zhang, L. Z.; Yu, J. G. *Chem. Mater.* **2002**, *14*, 4647−4653.
(46) Jain, A.; Toombes, G. E. S.; Hall, L. M.; Mahajan, S.; Garcia, C. B. W.; Probst, W.; Gruner, S. M.; Wiesner, U. *Angew. Chem., Int. Ed.* **2005**, *44*, 1226−1229.
(47) Cho, B. K.; Jain, A.; Gruner, S. M. *Science* **2004**, *305*, 1598−1601.
(48) Renker, S.; Mahajan, S.; Babski, D. T.; Schnell, I.; Jain, A.; Gutmann, J. S.; Zhang, Y. M.; Gruner, S. M.; Spiess, H. W.; Wiesner, U. *Macromol. Chem. Phys.* **2004**, *205*, 1021−1030.
(49) Thomas, A.; Schlaad, H.; Smarsly, B.; Antonietti, M. *Langmuir* **2003**, *19*, 4455−4459.
(50) Smarsly, B.; Grosso, D.; Brezesinski, T.; Pinna, N.; Boissiere, C.; Antonietti, M.; Sanchez, C. *Chem. Mater.* **2004**, *16*, 2948−2952.
(51) Weng, C. C.; Chen, P. P.; Ting, C. H.; Wei, K. H. *Chem. Mater.* **2005**, *17*, 3328−3330.
(52) Sun, Z. C.; Gutmann, J. S. *Physica A* **2004**, *339*, 80−85.
(53) Kim, D. H.; Sun, Z. C.; Russell, T. P.; Knoll, W.; Gutmann, J. S. *Adv. Funct. Mater.* **2005**, *15*, 1160−1164.
(54) Kim, D. H.; Kim, S. H.; Lavery, K.; Russell, T. P. *Nano Lett.* **2004**, *4*, 1841−1844.
(55) Groenewolt, M.; Brezesinski, T.; Schlaad, H.; Antonietti, M.; Groh, P. W.; Ivan, B. *Adv. Mater.* **2005**, *17*, 1158−1162.
(56) Steunou, N.; Forster, S.; Florian, P.; Sanchez, C.; Antonietti, M. *J. Mater. Chem.* **2002**, *12*, 3426−3430.
(57) Wang, H.; Oey, C. C.; Djurisic, A. B.; Xie, M. H.; Leung, Y. H.; Man, K. K. Y.; Chan, W. K.; Pandey, A.; Nunzi, J.-M.; Chui, P. C. *Appl. Phys. Lett.* **2005**, *87*, 023507.
(58) Discher, D. E.; Eisenberg, A. *Science* **2002**, *297*, 967−973.
(59) Choucair, A.; Eisenberg, A. *Eur. Phys. J. E* **2003**, *10*, 37−44.
(60) Burke, S.; Shen, H. W.; Eisenberg, A. *Macromol. Symp.* **2001**, *175*, 273−283.
(61) Soo, P.; Eisenberg, A. *J. Polym. Sci., Part B: Polym. Phys.* **2004**, *42*, 923−938.
(62) Zhang, L. F.; Eisenberg, A. *Polym. Adv. Technol.* **1998**, *9*, 677−699.
(63) Yu, Y. S.; Zhang, L. F.; Eisenberg, A. *Macromolecules* **1998**, *31*, 1144−1154.
(64) Zhang, L. F.; Eisenberg, A. *Macromolecules* **1996**, *29*, 8805−8815.
(65) Shen, H. W.; Eisenberg, A. *J. Phys. Chem. B* **1999**, *103*, 9473−9487.
(66) Burke, S. E.; Eisenberg, A. *Langmuir* **2001**, *17*, 8341−8347.
(67) Yu, K.; Eisenberg, A. *Macromolecules* **1996**, *29*, 6359−6361.
(68) Yu, K.; Eisenberg, A. *Macromolecules* **1998**, *31*, 3509−3518.
(69) Luo, L. B.; Eisenberg, A. *Langmuir* **2001**, *17*, 6804−6801.
(70) Liu, F. T.; Eisenberg, A. *J. Am. Chem. Soc.* **2003**, *125*, 15059−15064.

Scheme 1. Sample Preparation Procedure for TiO_2 Films with Varied Morphologies

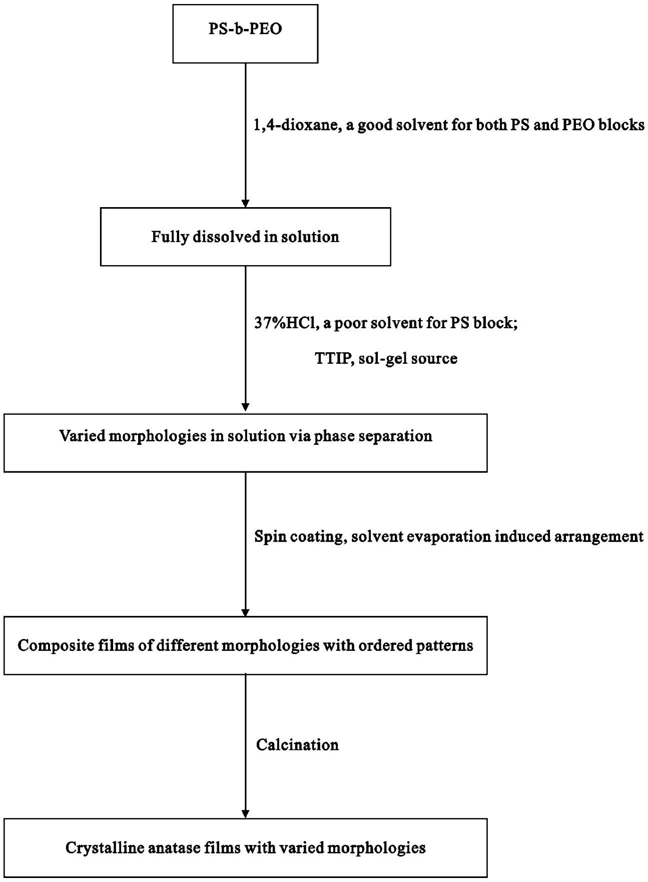

because TTIP can be incorporated into the hydrophilic PEO domains through coordination bonds. Furthermore, the hydrolysis and condensation of TTIP turn the PEO domains chemically reactive, as the titania species on the surface of the PEO domains are capable of forming covalent Ti−O bonds with other titania species on the surface of adjacent PEO domains. This is of special importance as the morphology of the micelles in solution is the result of a dynamic equilibrium in which micelles constantly fuse together and break apart. Consequently, permanent Ti−O− covalent bonds can be formed between neighboring PEO domains when two micelles fuse together. As a result of the complex force balance, different morphologies can be obtained by adjusting the relative weight fractions between 1,4-dioxane, HCl, and TTIP. Also, a micelle to reverse-micelle transition process in the solution is possible because the major solvent of 1,4-dioxane is a good solvent for both PS and PEO blocks, which expands the spectrum of the potential morphologies formed in solution. In many of the results that have been reported before, hydrophobic solvents were used as the major solvents, and as a result only micelles composed of hydrophilic cores and hydrophobic coronas were formed in the solution.[38−40,52,53] However, in our studies, 1,4-dioxane, a good solvent for both hydrophobic and hydrophilic blocks of the block copolymer, allows it to be possible to form either the PEO or PS core in the solution. As the last step of preparation, composite films containing organic block copolymer templates and inorganic Ti−O− functional parts are obtained on Si(100) substrates via spin coating. During this step a solvent evaporation induced arrangement process is possible in which the nanostructures within the films are arranged in an ordered fashion. As a result, homogeneous films composed of different morphologies in an ordered arrangement over mm^2 surface areas are accomplished.[71,72] Finally, crystalline TiO_2 films with different morphologies are obtained through calcination.

Experimental Section

An asymmetric diblock copolymer of polystyrene and poly(ethylene oxide) (PS-*b*-PEO) was obtained from Polymer Source Inc. The number average molecular weight is 19 kg/mol for PS and 6.4 kg/mol for PEO respectively, with a polydispersity of 1.05.

Titanium tetraisopropoxide (TTIP, 97%) was purchased from Aldrich. 1,4-Dioxane of analytical reagent grade was obtained from Fisher Scientific, and concentrated HCl (Puriss, p.a.) (min. 37%) was purchased from Riedel-de Haën.

Sample solutions were prepared according to the following procedure: 0.040 g of PS-*b*-PEO and 4.0 g of 1,4-dioxane were mixed together, followed by the addition of the appropriate amounts of 37% concentrated HCl solution and TTIP within 3 min. After complete addition the common solution was stirred for a period of time ranging from 30 min to 1 h.

To compare the morphologies of the composite films to the morphologies of the pure block copolymer, solutions of pure block copolymers were prepared with the same procedure except that no TTIP is added. The weight ratios of concentrated HCl solution over the sum of 1,4-dioxane and HCl solution is varied from 0% to 10%.

Films were prepared on Si(100) substrates by spin coating for 120.0 s using a Süss MicroTec Delta 80 spin coater under ambient conditions (temperature, 21 °C; relative humidity, 35-45%; rotation speed of 2000 rpm; acceleration speed of 2000 rpm/s; closed cover). To clarify the influence of humidity, samples were also spin coated with a speed of 2000 rpm at 22.0 °C and 0.0 ppm absolute humidity in a glovebox (P-6000 spin coater, Specialty Coating System Inc.). The film thickness was measured by a Tencor P-10 surface profiler.

Calcination of the films was carried out at 400 °C for 4 h in air with a heating rate of 6.25 °C/min starting from room temperature. After calcination, the samples were cooled to room temperature in the furnace. The effect of calcination temperature was studied on a series of samples. The samples were calcined at 400, 500, and 600 °C for 4 h, respectively, with an identical ramp of 6.25 °C/min. After calcination, the samples were cooled to room temperature in the furnace.

Samples for XRD measurement were prepared by adding a few drops of the solution onto 2.5 cm × 2.5 cm Si(100) substrate, allowing the solution to dry under ambient conditions. Then the films were calcined in air at 200, 400, 500, 600, and 800 °C for 4 h, respectively, with the same recipe as mentioned above.

AFM images were recorded using a Digital Instruments Dimension 3100 scanning force microscope in tapping mode equipped with Olympus cantilevers (spring constant ranging between 33.2 and 65.7 N/m and resonant frequency of 277.3−346.3 kHz). The images were analyzed using the software of Nanoscope 5.12r5.

Scanning electron microscopy (FESEM) images were obtained on a field emission SEM (LEO 1530 “Gemini”). The accelerating voltage was 1 kV if without special mention in the text. The FFT pattern was obtained using the Image J 1.33U software, and areas of 512 × 512 pixels of the SEM images were randomly selected and studied.

The $\theta-\theta$ measurements were conducted on a Siemens D500 diffractometer equipped with a Cu anode generated at a current of 30 mA and a voltage of 30 kV. Scans were taken in a 2θ range from 20° to 80° with a step size of 0.05° and integration time of 30.0 s.

---

(71) Sun, Z.; Wolkenhauer, M.; Bumbu, G. G.; Kim, D. H.; Gutmann, J. S. *Physica B* **2005**, *357*, 141−143.

(72) Sun, Z. C.; Kim, D. H.; Wolkenhauer, M.; Bumbu, G. G.; Knoll, W.; Gutmann, J. S. *ChemPhysChem* **2006**, *7*, 370−378.

DLS Experiment. A frequency-doubled, cw Nd:YAG laser (Coherent, model Verdi 2W) was used at $\lambda = 532$ nm and up to 150 mW of power on the sample cell. The scattering cell is mounted in the center of a goniometer (ALV, Langen, Germany) with all degrees of freedom adjustable. A Glan polarizer selects only vertically polarized incident light. The scattered intensity is detected through a single-mode optical fiber which contains a Y-coupler ending in two avalanche diodes (ALV, Langen, Germany) acting as single-photon detector setup. The detected, scattered light is computed to correlation functions by a hardware correlator (5000/E, ALV, Langen, Germany). The output of the two avalanche diodes (APD) enables us to do a pseudo-cross-correlation and by this to avoid the well-known after-pulsing of APDs leading to distortion of the correlation functions below 10 μs otherwise.

Results and Discussions

Morphologies of Pure Block Copolymer. Eisenberg and coworkers have intensively studied the crew-cut morphologies of amphilic block copolymer PS-*b*-PEO in solution. However, the polymers they used have extra short block of PEO.[61,67] Our block copolymer has a longer PEO chain than they used. Furthermore, they used DMF as a good solvent and water as a poor solvent. Here in our case, 1,4-dioxane is used as a good solvent and concentrated HCl as a poor solvent for the PS block. Because our studies are focused on films spin coated on Si substrates, we prepare films of pure PS-*b*-PEO on Si substrates and study the morphologies with SEM or AFM, instead of studying the morphologies in solution. The results obtained on pure block copolymer films can thus be easily related to the morphologies of titania−block copolymer composite films.

The solutions with concentrated HCl ratios up to 2.84% are clear. With higher ratios the solutions become turbid, indicating the formation of micrometer-sized aggregates in the solution.

For the films without acid and with 1.06% concentrated HCl, it is difficult to characterize the films with SEM because of the small sizes of the structures. As an alternative way, AFM in tapping mode is used to study the morphologies of the films.

From AFM, cylinder-like structures can be observed. The spacing size between nanowires derived from power spectral density profiles are 22 nm for both films.

With the HCl amount increased to 2.08%, nanowire structures can be seen in the SEM image (Figure 1c). However, besides nanowires, lamellae structures are also present in the film. When the HCl content is further increased to 2.84%, the amount of nanowire structures is increased and the nanowires are partially covered by lamellae structures (Figure 1d). When the concentrated HCl solution weight ratio is 4.09% (Figure 1e) and 4.96% (Figure 1f), vesicle structures appear in the film, coexisting with the nanowire structures. With HCl content further increased to 5.97% (Figure 1g) and 6.92% (Figure 1h), vesicles of large size are formed. Huge size vesicles and a large number of small-sized vesicles are present at HCl concentrations of 8.05% (Figure 1i), 8.92% (Figure 1j), and 9.88% (Figure 1k).

The morphologies formed by pure block copolymer are similar to those present in the composite films, which will be discussed in the main part of this article. This similarity confirms the templating effect of block copolymer to control the morphologies of the titania nanostructures.

Phase Diagram. Figure 2 shows the phase diagram indicating the existence region of different morphologies. The morphologies are formed by simply varying the relative weight fractions between 1,4-dioxane, 37% HCl, and TTIP. They include clustered nanoparticles, flakelike structures, nanowires and nanowire aggregates, nanodoughnut structures, collapsed vesicles, nanogranulas, wormlike aggregates, and foamlike structures.

In terms of composition, the phase space in which templated nanostructures are formed is limited by the amount of HCl solution. Micrometer-sized precipitates of the block copolymer will appear in the solution at a weight fraction (W_{HCl}) larger than 0.1. The same holds true for a TTIP weight fraction larger than 0.1, where films with a large number of cracks are formed. For this reason only the compositional region of the phase diagram shown in Figure 2 is further investigated in this paper. The individual morphologies formed within the investigated compositional region and their associated structure formation mechanisms are discussed in the following.

Clustered Nanoparticles. With very low weight fractions of both HCl (less than 0.005) and TTIP (from 0.005 to 0.02), clustered nanoparticles are formed. Figure 3, parts a and c, shows the AFM and SEM images of the clustered nanoparticles before calcination, respectively (film thickness: 38 nm). The SEM image of the morphologies after calcination is shown in Figure 3d.

The ringlike FFT patterns of the images before and after calcination indicate that the nanoparticles are of a defined size but random with respect to an orientation of their superstructure. Before calcination, the average center-to-center distance obtained from the AFM image is 41 nm, which is in agreement with the value from the SEM image (42 nm). After calcination, the center-to-center distance is 45 nm. When the PS-*b*-PEO block copolymer is dissolved in 1,4-dioxane, which is a good solvent for both PS and PEO blocks, the block copolymer will be fully dissolved and there are no self-assembly aggregates present in the solution. Along with the addition of concentrated HCl solution into the block copolymer solution, the interfacial energy between the PS block and solvent system is increased because the HCl solution is a poor solvent for the PS block.

To minimize the extra surface free energy, a spherical micelle structure is formed with a core of PEO block and corona of PS block. HCl solution and TTIP are incorporated into the hydrophilic PEO core, where TTIP is hydrolyzed and condensed into Ti−O− nanostructures. In solution, the spherical micelles may fuse together statistically, and as a result of fusion, the cores of the micelles will be linked together through the condensation process of Ti−O− nanostructures between neighboring cores.

This linking process is, however, irreversible because of the formation of covalent bonds. Consequently, the linkages between the neighboring micelles are fixed and clustered nanoparticles are formed in the solution. The presence of micelle aggregates in solution can be confirmed by dynamic light scattering results (Supporting Information Figure S-1). After spin coating, composite films composed of clustered nanoparticles are obtained on the Si(100) substrate, which are proved in Figure 3c. By comparing the SEM images before and after calcination (Figure 3d), it can be concluded that the clustered nanoparticle structures are retained after calcination.

Flakelike Structures. Figure 4, parts b and c, shows a flakelike structure before and after calcination (film thickness before calcination, 41 nm). With increasing weight fraction of HCl, the interfacial surface energy is further increased, and in

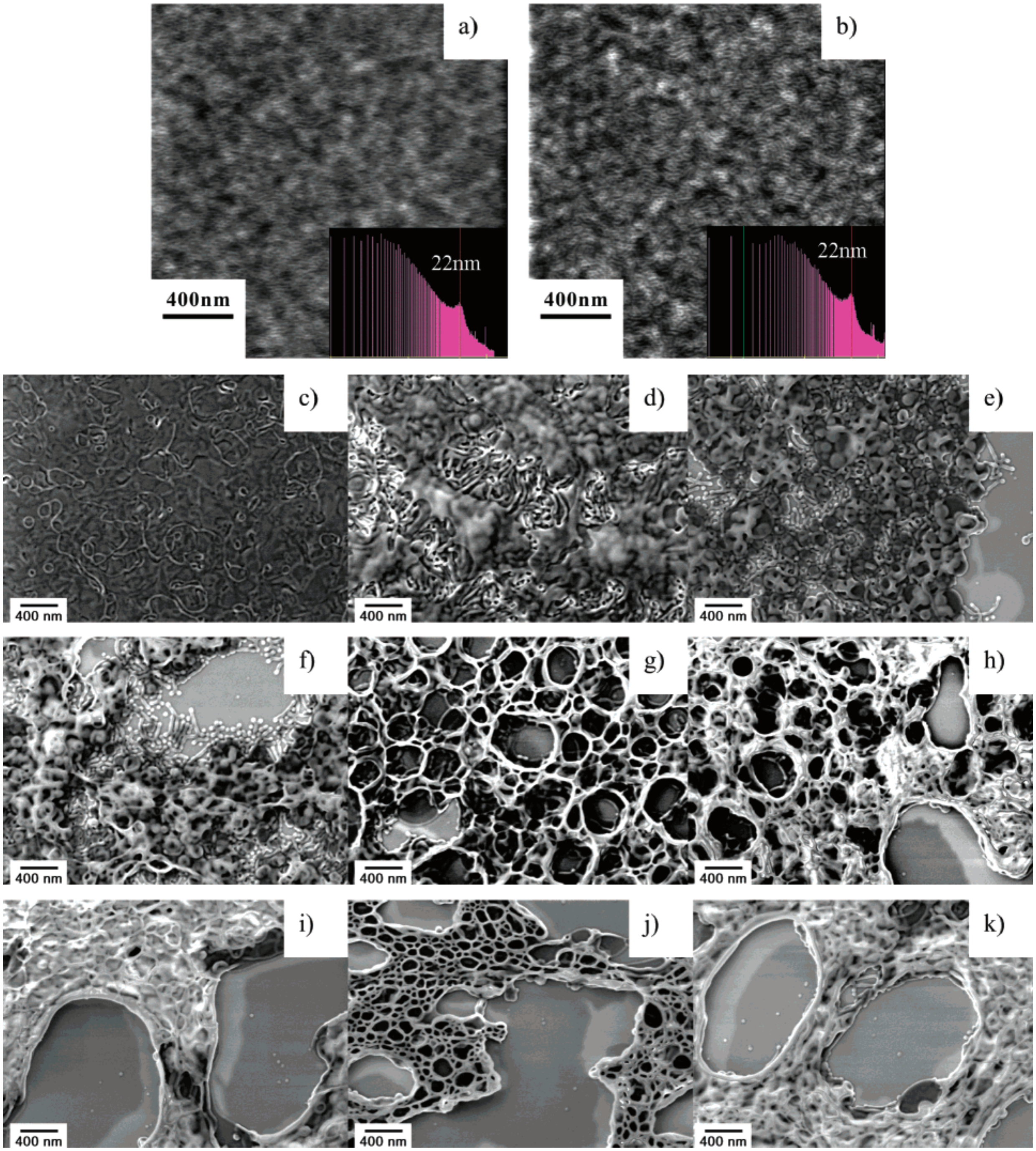

Figure 1. AFM (a and b) height images and SEM images of the films spin coated from pure PS-*b*-PEO block copolymer in 1,4-dioxane with increasing weight ratios of concentrated HCl solution. $W_{\mathrm{HCl/(HCl+1,4-dioxane)}}$ is 1.06%, 2.08%, 2.84%, 4.09%, 4.96%, 5.97%, 6.92%, 8.05%, 8.92%, and 9.88% for samples in panels a−k, respectively. The height scale of the AFM images is 5 nm. The insets in images a and b are power spectral density profiles of their corresponding AFM images.

order to lower the surface energy, the clustered spherical micelles grow into isolated flakes with sizes ranging from tens to a few hundred nanometers. The flakes are actually three-dimensional structures, as from SEM images it can be seen that the peripheral of the flakes extrude from the flake plane. Similar flakelike structures were also observed by Yu and Eisenberg in the solution of pure PS-*b*-PEO in DMF, where a so-called lamellae structure with protruding nanorods was formed.[67,68] The flakelike morphologies are also present in pure PS-*b*-PEO films (Figure 1c and 1d), indicating the templating effects of the block copolymer.

Nanowires and Nanowire Aggregates. Figure 5, parts a and c, shows the AFM phase image and SEM image of the nanowire structures before calcination, respectively (film thickness before calcination, 33 nm). Figure 5d shows the SEM image of the nanowire structures after calcination. From the AFM image in Figure 5a it can be seen that the titania−block copolymer composite nanowires are arranged in parallel over large length scales, which is also seen in the SEM image in Figure 5c. The average spacing size of the nanowires is 51 nm according to the FFT pattern of the AFM image, which is in accordance with the value obtained from the SEM image (52 nm). What is

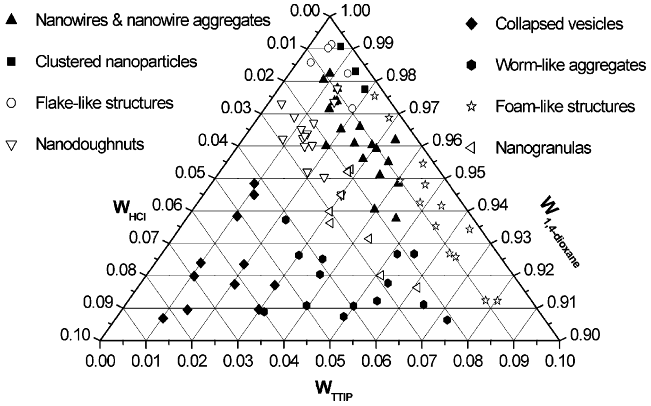

Figure 2. Phase diagram of TiO_2 films after calcination with varied morphologies (W, weight fraction).

interesting is that both the AFM and the SEM images before calcination show double ringlike FFT patterns. While the inner ring can be assigned to the spacing between neighboring nanowires, the outer ring corresponds to the second order of the first ring. From the presence of the second-order ring we conclude that the nanowires are closely packed leading to a strong ordering in a bundle consisting of several nanowires. For the SEM image in Figure 5d, no clear ringlike FFT pattern can be observed, indicating a loss of order after calcination. The average diameter of the nanowires is 27 nm, which is significantly smaller than the size before calcination. We assume that the cylinder micelles are formed in the solution from a comparison of our system with Eisenberg's reported results, where an amphilic block copolymer of PS-*b*-PAA is used and 1,4-dioxane is applied as a good solvent for both the PS and the PAA blocks and water as a poor solvent for the PS block.[58−62,65,66] They obtained and proved the existence of cylinder micelles in the solution. In our case, instead of PS-*b*-PAA, another amphilic block copolymer of PS-*b*-PEO is used, which we assume to behave qualitatively similarly as PS-*b*-PAA in solution. Although there is additional TTIP in the copolymer solution, which is different from Eisenberg's results, we believe that the nanowires within the films cannot be formed directly from the spin-coating process if there is no cylinder structure initially formed in the solution. Furthermore, nanowire structures composed of pure PS-*b*-PEO polymer are observed in the copolymer film (Figure 1c−f), which means that the copolymer does act as a template to control the formation of composite nanowire structures.

The formation mechanism of the titania−block copolymer nanowires can be understood as the following. With increasing amount of concentrated HCl solution, the solvent is becoming more and more poor for the PS block leading to a continuously rising surface energy between the PS block and the solvent. To minimize the surface free energy, the spherical micelles will change shape to decrease the specific surface area, leading to the formation of cylinder micelles in the solution. Besides the HCl solution, the increasing amount of TTIP in the PEO core domains also makes a contribution to the morphology transformation because the hydrolysis and condensation of TTIP will release 2-propanol at the price of water consumption, which is also a poor solvent for the PS block. The overall reaction of hydrolysis and condensation leads to the net amount increase of hydrophilic solvent in the solution, which makes the solvent system increasingly poor for the PS block.[73]

In AFM measurements different positions on the film were checked, and the images recorded in different positions show comparable morphologies. SEM images at low magnification show that the surface is homogeneously covered with ordered nanowires (See Supporting Information Figure S-2). Therefore, we are confident to conclude that the homogeneous films composed of ordered nanowire structures cover the surface of a mm^2 scale.

After calcination, the organic block copolymer is burned off and only titania is left. From the SEM image after calcination, it can be seen that the nanowire structures are retained, which further confirms the existence of cylindrical micelles. By comparing the SEM images before and after calcination, we can find that the nanowires before calcination are arranged very tightly. However, after calcination, big gaps between the neighboring nanowires can be seen in the SEM image. This phenomenon corroborates our structural picture of the corona composed of PS. After calcination the coronas of the nanowires are burned away and gaps appear between neighboring nanowires. The assumption that the cylinder micelles have PS coronas can be proved by four facts: First, the SEM image before calcination has a lower contrast compared to that of the SEM image after calcination, indicating the presence of an organic block copolymer coverage on the nanowires before calcination. Second, in the SEM image after calcination, most of the nanowire structures are separated and only very minor parts of the nanowires are seemingly bound together. If the composite nanowires had an outer PEO corona, then the Ti−O− species within the PEO domains would tend to bind together during calcination due to the thermal driving force. Third, the size of the calcined nanowire structures is significantly decreased compared to that of the nanowire structures before calcination. Fourth, if PS blocks would form the nanowire cores, there would be porous structures formed after calcination because the inner PS cores would be totally burned off. However, the calcined structures obtained are solid nanowires and nanotubular-like structures are not observed. Therefore, based on the above-mentioned facts and discussions, we conclude that the composite nanowires have a core composed of PEO blocks and corona composed of PS blocks.

With increasing weight fraction of TTIP and fixed weight fraction of HCl, we can observe an interesting phenomenon of the titania nanowire structure evolution (see Figure 6). The weight fraction of HCl is fixed at 0.01, and the weight fraction of TTIP is varied from 0.01 to 0.04. For the sample with a TTIP weight fraction of 0.01, well-ordered nanowire structures are present in the film and there are almost no other side morphologies coexisting in the film (Figure 6, panels a1 and a2). It is actually the sample shown in Figure 5. The sizes of the nanowires are uniform not only within a single nanowire, but also for different nanowires, which reflects the highly uniform characteristics of the cylinder micelles in solution. The double ringlike FFT pattern of the SEM image also indicates high order of the nanowire structures, and the average spacing size of the nanowires is found to be 52 nm from the FFT pattern. After

---

(73) Papoutsi, D.; Lianos, P.; Yianoulis, P.; Koutsoukos, P. *Langmuir* **1994**, *10*, 1684−1689.

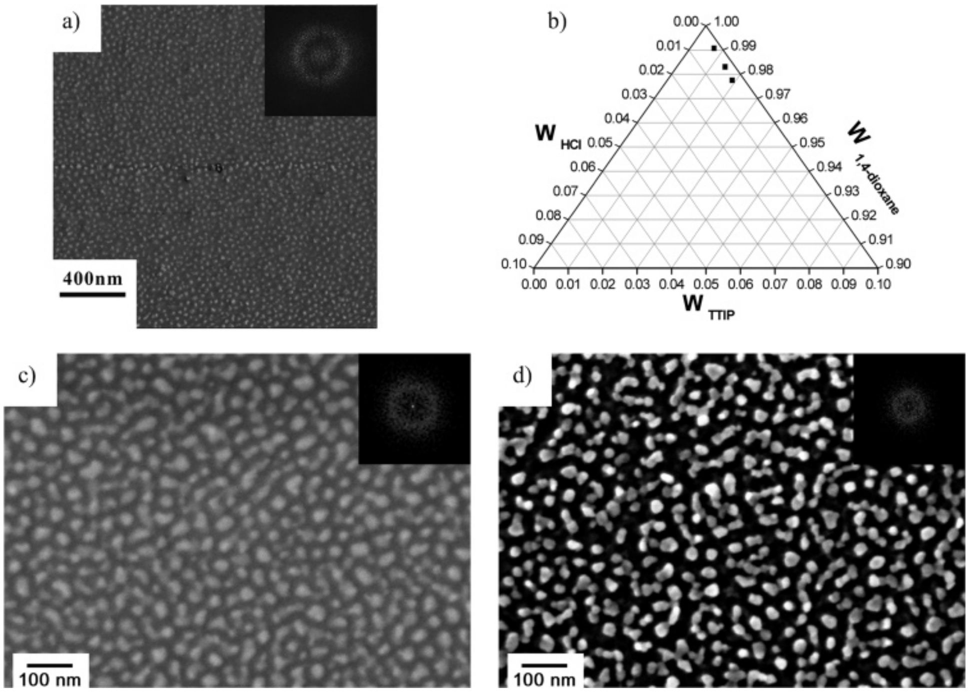

Figure 3. AFM and SEM images of TiO_2 films with clustered nanoparticles. (a) AFM phase image before calcination; phase scale, 10°. (b) Compositional existence region in the phase diagram (*W*, weight fraction). (c) SEM image before calcination. (d) SEM image after calcination. The insets in the images are FFT patterns of the corresponding structures.

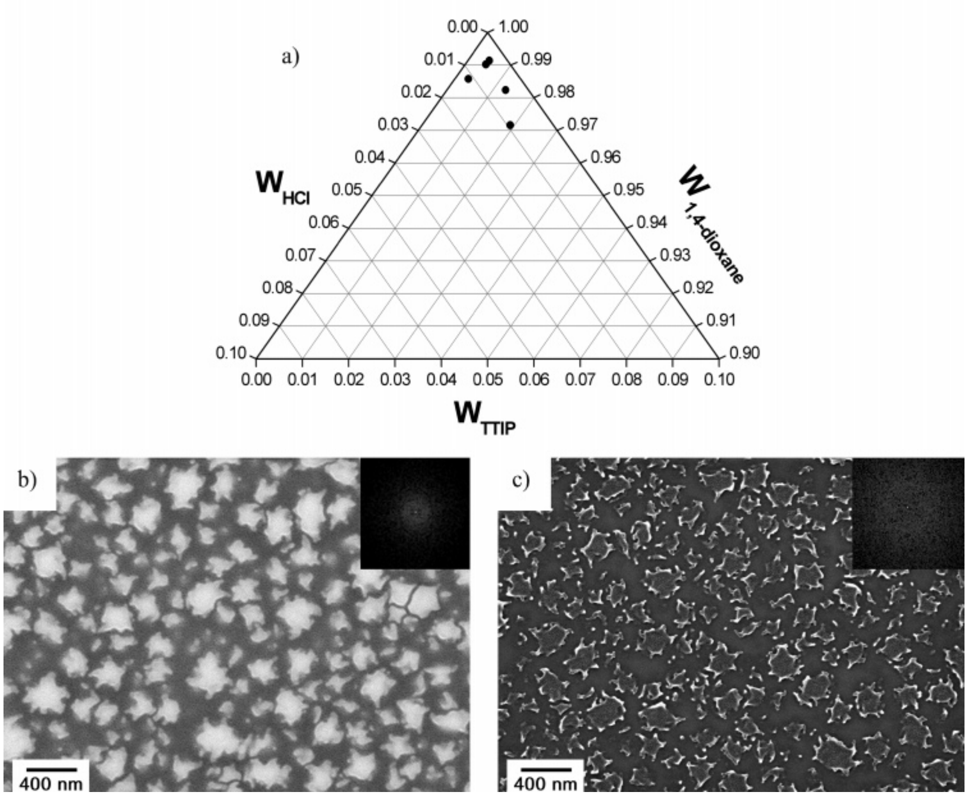

Figure 4. AFM and SEM images of TiO_2 films with flakelike morphologies. (a) Compositional existence region in the phase diagram (*W*, weight fraction). (b) SEM image before calcination. (c) SEM image after calcination. The insets in the images are FFT patterns of the corresponding structures.

calcination the morphologies of TiO_2 are almost purely nanowires, reflecting the corresponding structures before calcination.

When the TTIP weight fraction is increased to 0.015 (film thickness, 41 nm before calcination), it can be seen that the order degree of the nanowires is decreased compared to that of the sample in Figure 6a and the size of the nanowires is no longer uniform (Figure 6, panels b1 and b2).

In the image Figure 6b1 there are some nanowires with obviously larger sizes than other nanowires, and there are also some nanowires featuring nodular structures. The outer ring in

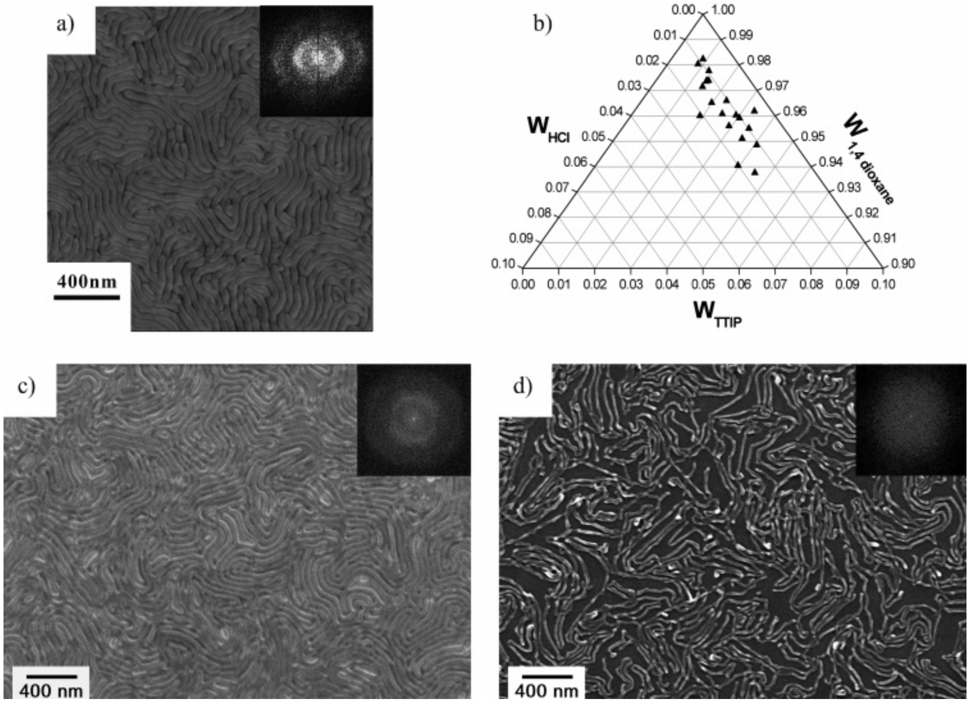

Figure 5. AFM and SEM images of TiO$_2$ films with nanowires. (a) AFM phase image before calcination; phase scale, 20°. (b) Compositional existence region in the phase diagram (W, weight fraction). (c) SEM image before calcination. (d) SEM image after calcination. The insets in the images are FFT patterns of the corresponding structures.

the FFT pattern is broadened compared to that of the first sample, indicating less order of the nanowire structures in the film. The spacing size of the nanowires averaged from the inner ring of the FFT pattern is 52 nm, which is in agreement with the sample in Figure 6a. Besides the main morphologies, there are some vesicle-like structures coexisting in the film, which will be discussed later. For the structures obtained after calcination, we can still see some nanowires containing nodules, reminiscent of the protrusion features in the nanowires before calcination.

For the sample with a TTIP weight fraction of 0.025 (film thickness before calcination, 35 nm), many nanowire structures are forked (Figure 6, panels c1 and c2). It can also easily be seen from the SEM image before calcination that the nanowire structures stack as a multilayer, and a ringlike FFT pattern is still present before calcination. The corresponding spacing size between nanowire structures is 51 nm. After calcination, TiO$_2$ nanowire structures with a large number of junctions are obtained. When the weight fraction of TTIP is further increased to 0.030 (film thickness before calcination is 43 nm), the number of junctions is further increased compared to that of the sample with a TTIP weight fraction of 0.025 (Figure 6, panels d1 and d2). The ringlike FFT pattern of the image before calcination is further broadened compared to that of the samples with lower TTIP weight fractions, and the average spacing between the nanowires is about 42 nm, which is smaller than the first three samples in the series. After calcination, both nanowires and junctions are retained and a mesoscale network structure is formed. It can be found that the morphologies before and after calcination correspond very well. When the weight fraction of TTIP reaches 0.040 (film thickness before calcination, 46 nm), there are many junctions of different sizes in the film and the nanowires are not the dominant structural elements any more (Figure 6, panels e1 and e2). The ringlike FFT pattern in the SEM image before calcination is rather broadened, and the spacing of the nanowire structures is further decreased to roughly 33 nm. After calcination, a TiO$_2$ mesoscale network composed of nanowires and junctions is obtained.

From the structure evolution it can be found that the morphologies evolve from pure nanowires via interconnected nanowires to mesoscale network structures due to an increasing amount of junctions in the film. The mechanism of the morphology evolution can be rationalized by analyzing the role of TTIP in the system because for the above five samples, the relative weight fraction of HCl is always kept constant. The micelle core is chemically reactive because the Ti−O− nanostructures inside the core can undergo further condensation with neighboring cores, and the potential for further condensation is increased with increasing weight fraction of TTIP. Being mobile in solution, cylinder micelles may come close to each other and fuse together, which in pure block copolymer micelles is a statistical and dynamic event. However, in our system case, the cores will be linked covalently through the condensation of Ti−O− nanostructures between each other as a result of the micellar fusion. The increasing amount of TTIP in the micelle cores introduces more possibilities of the formation of linkages between cylinder micelles. Consequently, the number of junctions is increased with increasing W_{TTIP}.

In comparison to TTIP, an increase in the weight fraction of HCl retains the nanowire morphologies, where W_{TTIP} is 0.035 and W_{HCl} is 0.015 (Figure 7) (film thickness before calcination, 57 nm). The ringlike FFT patterns before calcination correspond to a characteristic spacing of 38 nm. If we only consider the effect of TTIP, the morphology should lie in the transition from Figure 6d to Figure 6e. However, from Figure 7 it can be seen that the number of the junctions is even less than that in Figure 6d. As the increasing weight fraction of HCl solution retards the condensation of Ti−O− nanostructures, it also hinders the

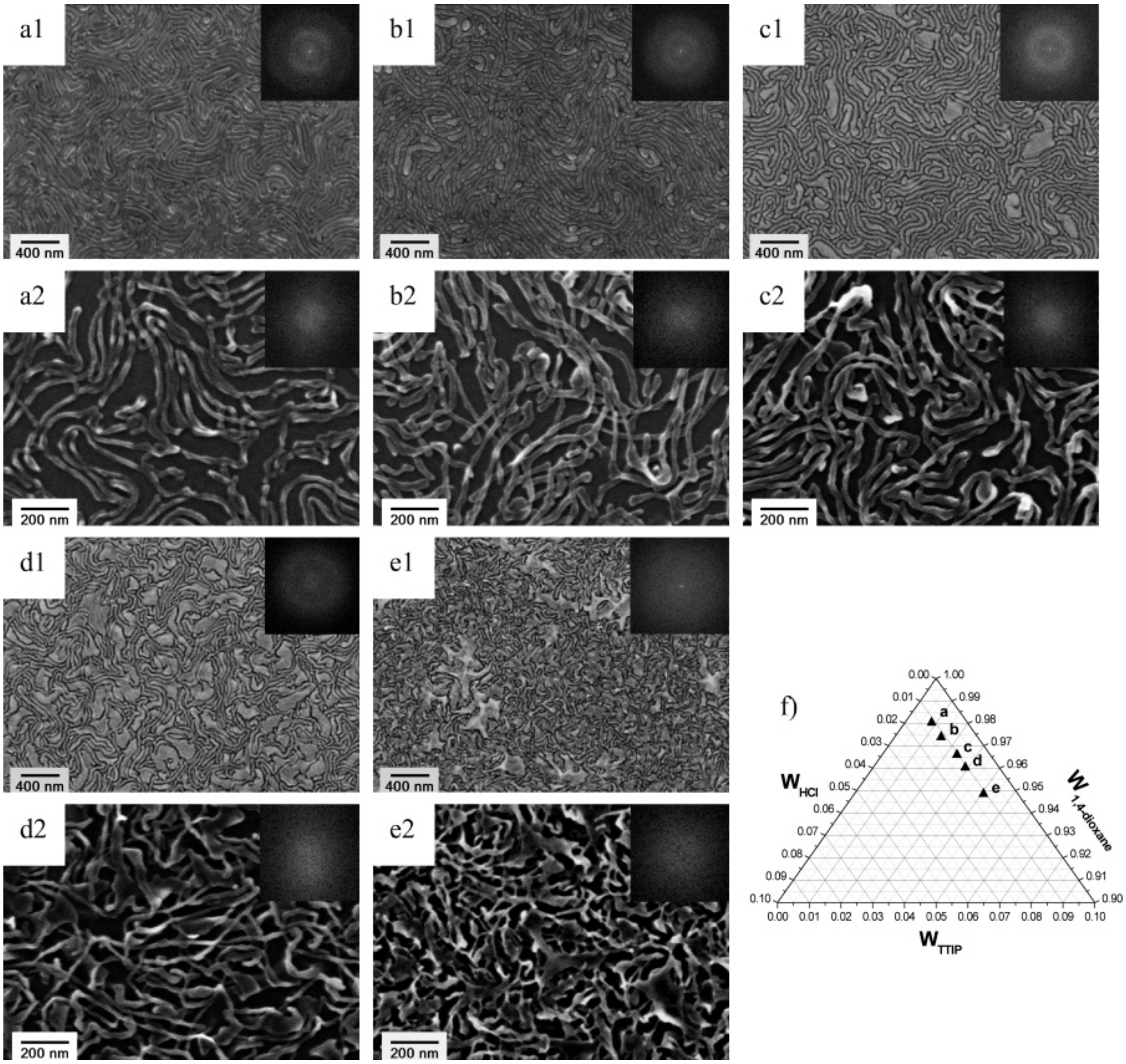

Figure 6. SEM images of structure evolution with increasing weight fractions of TTIP in TiO_2 nanowire films. Panels a1−e1: SEM images before calcination. Panels a2−e2: SEM images after calcination. Panel f: compositional existence points in the phase diagram with increasing TTIP weight fractions from a to e (*W*, weight fraction). The insets in the images are FFT patterns of the corresponding structures.

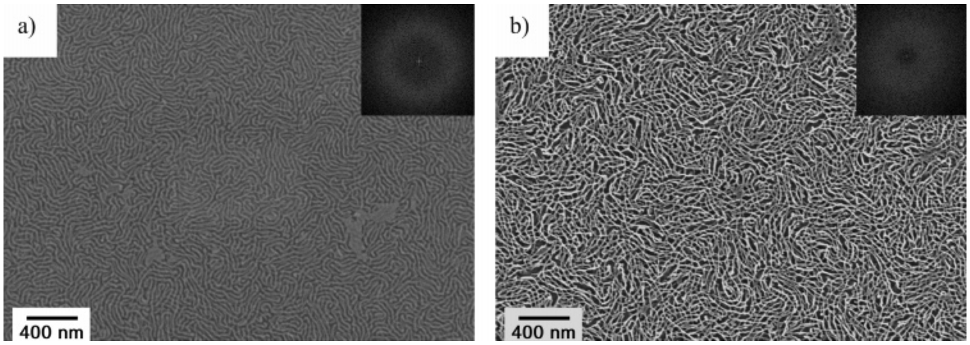

Figure 7. SEM images of TiO_2 films with nanowire structures before (a) and after (b) calcination. The insets in the images are FFT patterns of the corresponding structures.

formation of permanent junctions between neighboring nanowires, resulting in a reduced number of junctions under identical preparation conditions.[74]

Vesicle Structures. With a further increase in the weight fraction of concentrated HCl solution, the nanowire structures will transform into vesicles. The shape and size of the vesicles will be determined by two factors: the volume ratio of HCl to the total amount of PS-*b*-PEO, 1,4-dioxane, and TTIP will determine the overall size of the vesicles, while the volume ratio of TTIP to the volume of PEO in PS-*b*-PEO will determine the thickness of the titania shell of the vesicles. In our experiment, the amounts of PS-*b*-PEO and 1,4-dioxane were always kept

---

(74) Murakami, Y.; Matsumoto, T.; Takasu, Y. *J. Phys. Chem. B* **1999**, *103*, 1836−1840.

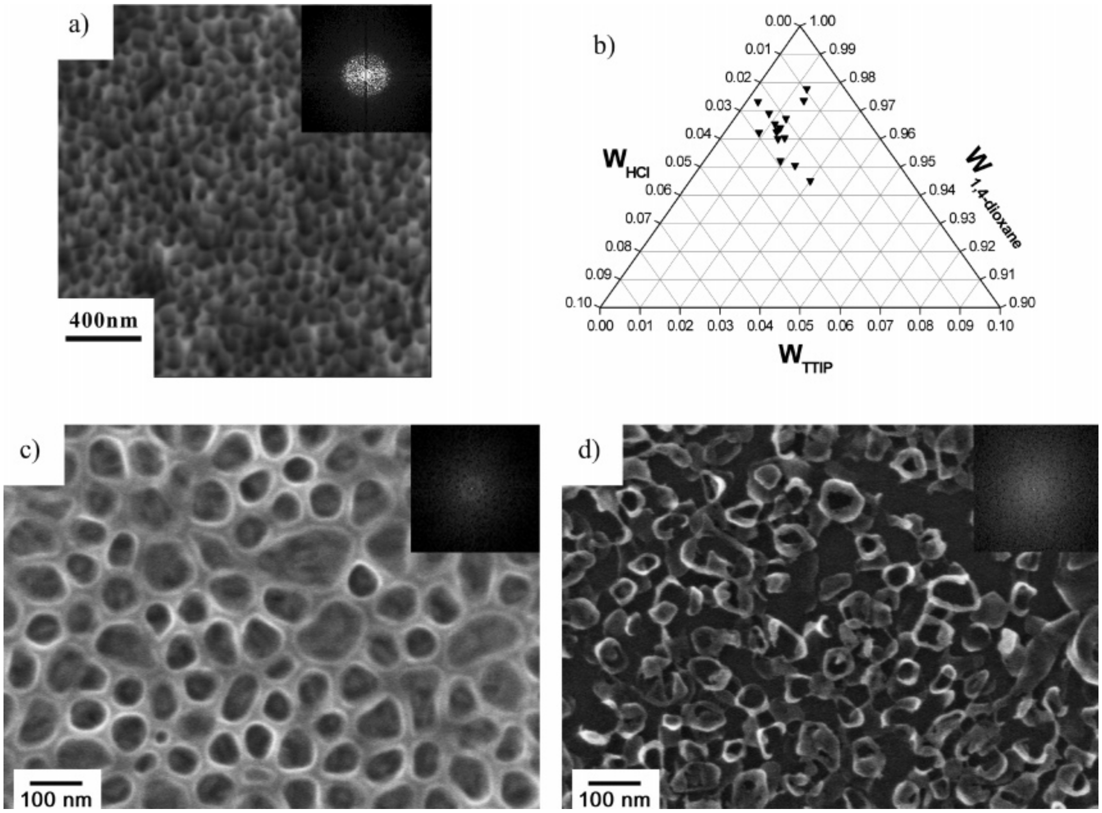

Figure 8. AFM and SEM images of TiO_2 films with nanodoughnuts. (a) AFM height image of the nanodoughnut structures before calcination; height scale, 40 nm. (b) Compositional existence region in the phase diagram (*W*, weight fraction). (c) SEM image before calcination. (d) SEM image after calcination. The insets in the images are FFT patterns of the corresponding structures.

constant; therefore, the morphology of the vesicle structures can be indicated by the relative weight fractions of HCl and TTIP. We assume that the TTIP component gets incorporated into the wall of the vesicles and eventually integrated via condensation since the titania is complexed to the PEO domain. The vesicle structures can be divided into three subgroups according to their specific morphologies either directly present in the film, for example, nanogranulas, or after calcination, for example, nanodoughnuts and collapsed vesicles. The reason for the presence of different morphologies is due to varied ratios of vesicle size to wall thickness, which can be modified by the weight fractions of HCl and TTIP in the solution.

Nanodoughnut Structures. Figure 8, parts a and c, shows AFM and SEM images of the vesicle structures before calcination, respectively (film thickness, 49 nm). After calcination, a three-dimensional nanodoughnut structure is formed, which is shown in Figure 8d. A ringlike FFT pattern of the SEM image before calcination indicates the average spacing size of the vesicles is 73 nm, which is in agreement with the value obtained from AFM (71 nm). It is noteworthy that the three-dimension characteristic reminiscent of very uniform vesicular structures can even be seen in the AFM image.

A similar morphology transition trend was also observed by Choucair and Eisenberg, where PS-*b*-PAA in water solution can undergo the morphology transformation from nanowires to vesicles with increasing water amount.[59] Here in our case the amount of concentrated HCl solution is increased leading to an increase in surface free energy between the PS blocks and surrounding solvents, which drives the morphology transformation from nanowires to vesicles in order to minimize the extra interfacial surface energy. During spin coating the vesicles formed in the solution are rearranged in an ordered fashion on the Si wafer substrate via a solvent evaporation induced arrangement process.

Collapsed Vesicles. With increasing weight fraction of the concentrated HCl solution and constant W_{TTIP} compared to that of the nanodoughnut samples, the vesicle structures still remain present in the film (Figure 9b) (film thickness before calcination, 56 nm).

However, the vesicle structures are different from the nanodoughnut structures in two aspects: first, the average size of the vesicles is larger than the nanodoughnut structure; second, the ratio of vesicle size to wall thickness is increased. The increasing amount of HCl solution induces the formation of vesicles with large sizes to decrease the specific surface area. Vesicles with sizes of more than 200 nm are due to the fusion of several small vesicles. In comparison to the enlarged vesicle size, the wall thickness is nevertheless not increased, as the amount of TTIP swollen in the wall region of the vesicles is almost kept constant relative to that of the nanodoughnut samples. After calcination, the vesicle structures collapse into disordered structures because of the increasing ratio of vesicle size to wall thickness, which turns the vesicle structures unstable during calcination. However, some parts of the vesicle walls can still be observed on the substrate after calcination, reminiscent of the vesicle structures before calcination (Figure 9c).

Nanogranulas. Figure 10a shows the AFM image of nanogranulas before calcination, and Figure 10c shows the corresponding SEM image (film thickness before calcination, 64 nm). Figure 10d shows the SEM image of nanogranulas after

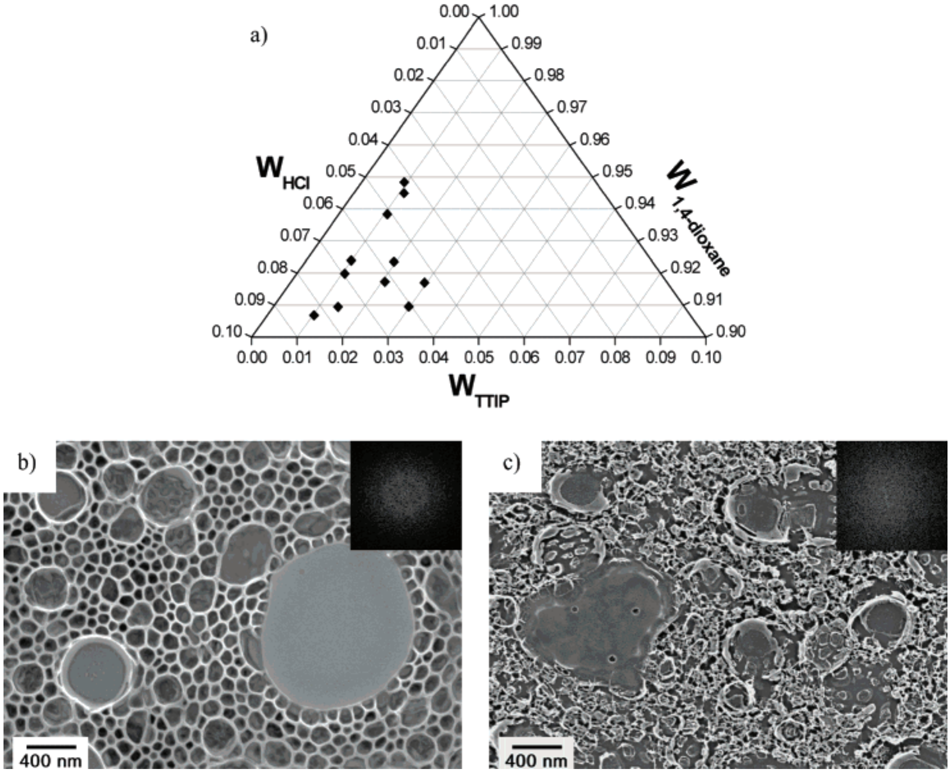

Figure 9. SEM images of TiO_2 films with collapsed structures after calcination. (a) Compositional existence region in the phase diagram (*W*, weight fraction). (b) SEM image before calcination. (c) SEM image after calcination. The insets in the images are FFT patterns of the corresponding structures.

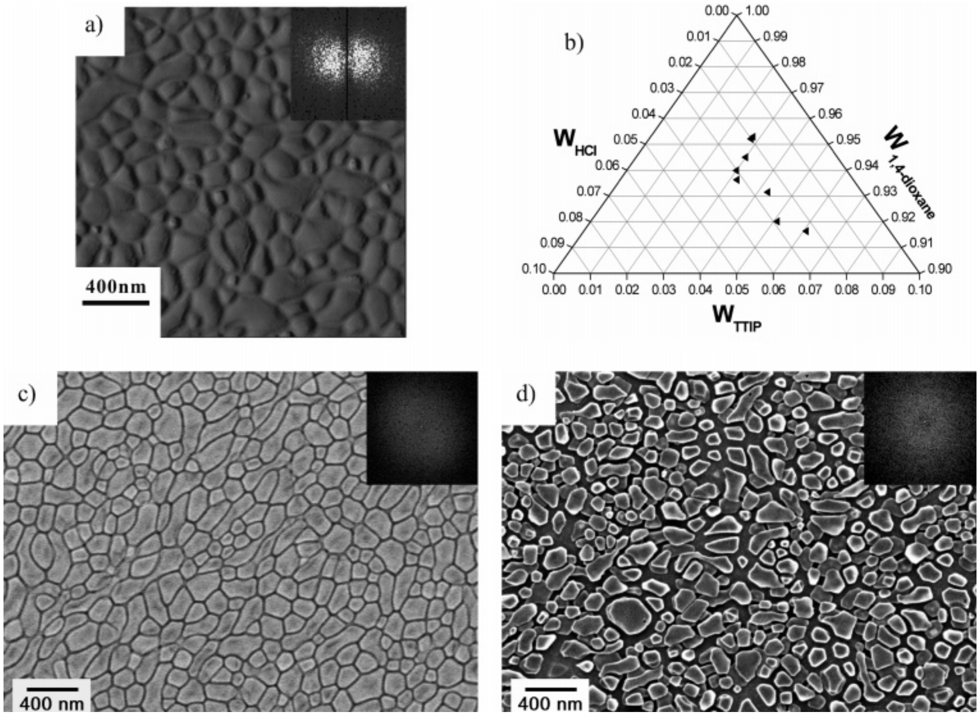

Figure 10. AFM and SEM images of TiO_2 films with nanogranula structures. (a) AFM phase image before calcination; phase scale, 30°. (b) Compositional existence region in the phase diagram (*W*, weight fraction). (c) SEM image before calcination. (d) SEM image after calcination. The insets in the images are FFT patterns of the corresponding structures.

calcination. The formation mechanism of the nanogranulas can be understood with the starting point of the vesicle structures. In comparison to the nanodoughnut sample, the increasing amount of TTIP will thicken the wall of the vesicles; however, the overall size of the vesicles are not increased correspondingly because the W_{HCl} remains constant. As a consequence of the combined effects of HCl and TTIP, the ratio of vesicle size to wall thickness is decreased.

The vesicle structures with thick walls are squashed into nanogranulas during spin coating because the solution is dried

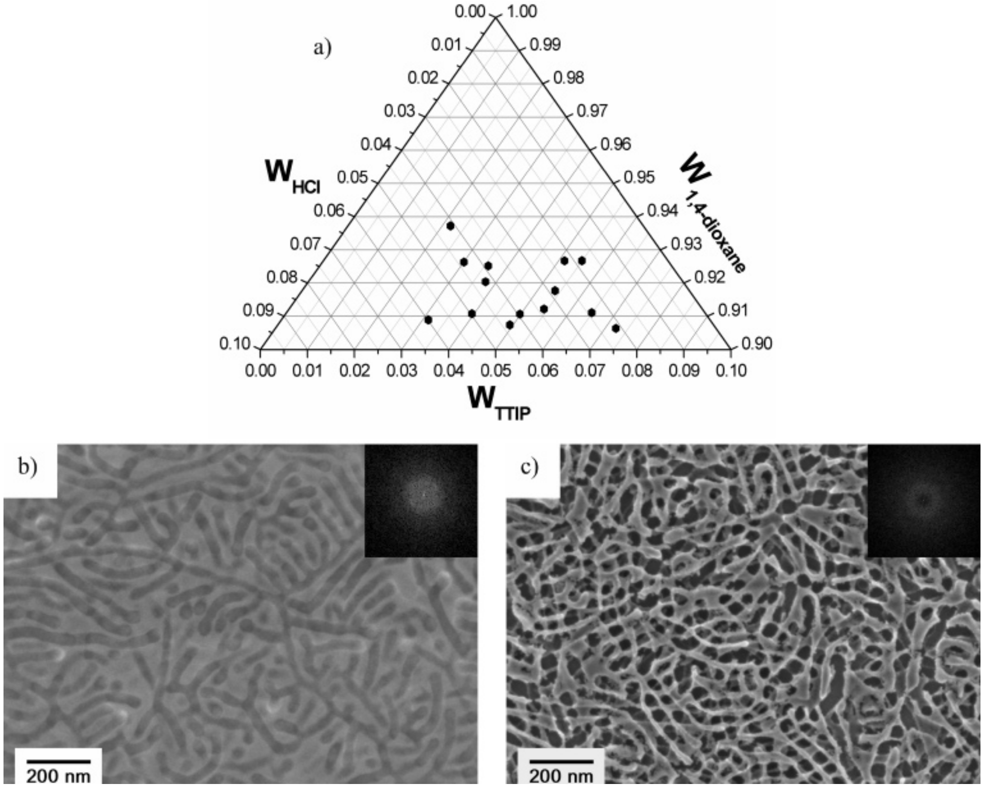

Figure 11. SEM images of TiO_2 films with wormlike aggregates before and after calcination. (a) Compositional existence region in the phase diagram (*W*, weight fraction). (b) SEM image before calcination. (c) SEM image after calcination. The insets in the images are FFT patterns of the corresponding structures.

and compressed to form an ultrathin film. The small depressed regions on the surface of the granular structures confirm the original vesicle structures.

Wormlike Aggregates. Figure 11, parts b and c, shows the SEM images of wormlike aggregates before and after calcination (film thickness before calcination, 55 nm).

Both SEM images show ringlike FFT patterns, and the corresponding characteristic spacing sizes are 44 and 43 nm, respectively, which means that the sizes of the structures are unchanged after calcination. However, there are holes present in the SEM image after calcination, whose formation mechanism will be discussed in the following.

Because of the increasing amount of hydrophilic solvents the surface energy between the PS blocks and solvents exceeds the stabilization energy limit of the micelles, and the micelle structures are no longer stable. As a result, an interesting phase transition from micelles to reverse micelles happens in the solution. The wormlike aggregates are inverted cylinder micelles consisting of PS cores and PEO coronas. TTIP and HCl solution are incorporated into the PEO coronas, and therefore a continuous phase is formed in which TTIP is hydrolyzed and condensed into Ti−O nanostructures. The assumption of the inverted cylinder micelles can be proved by analyzing the SEM images. First, there are holes present in the SEM image after calcination consistent with the removal of cylinder micelle cores composed of PS blocks after calcination. Second, the size of the wormlike structures remains constant in contrast to the significant size decrease in the nanowire samples, where the cylinder micelle coronas composed of PS blocks are burned off during calcination.

Foamlike Structures. Figure 12, parts b and c, shows the SEM images of foamlike structures before and after calcination (film thickness before calcination, 91 nm). It can be seen that the foamlike structures are basically formed in the region of the phase diagram with low weight fractions of HCl solution (Figure 12a).

The foamlike structures are composed of a skeleton containing large number of small-sized structures. The low amount of concentrated HCl solution makes it possible to form large amount of small-sized microphase-separated structures in the solution. And the high amount of TTIP incorporated into the PEO domains makes the PEO domains highly chemically reactive. It can undergo further hydrolysis and condensation reactions with other PEO domains when they are getting close induced by mutual collision, which is highly frequent in the solution because of the presence of the large amount of small structures. As a result, three-dimensional random structures composed of mutually linked small-sized structures are formed, which have a large specific surface area, leading to the formation of foamlike structures after calcination.

Summary of the Morphology Evolution. The total structure evolution in the investigated phase diagram can be summarized as follows. With low weight fractions of concentrated HCl solution and TTIP, clustered spherical micelles are formed in the solution (Figure 13, panels a1 and a2). The clustered spherical micelles can be transformed into diverse morphologies under different conditions. For example, with slightly higher weight fractions of HCl solution and comparable weight fractions of TTIP, flakelike structures are formed (Figure 13, panels b1 and b2). When the weight fraction of HCl solution is kept below 0.01 and the amount of TTIP is increased, a skeleton composed of a large amount of small-sized structures is formed leading to the formation of foamlike structures after calcination.

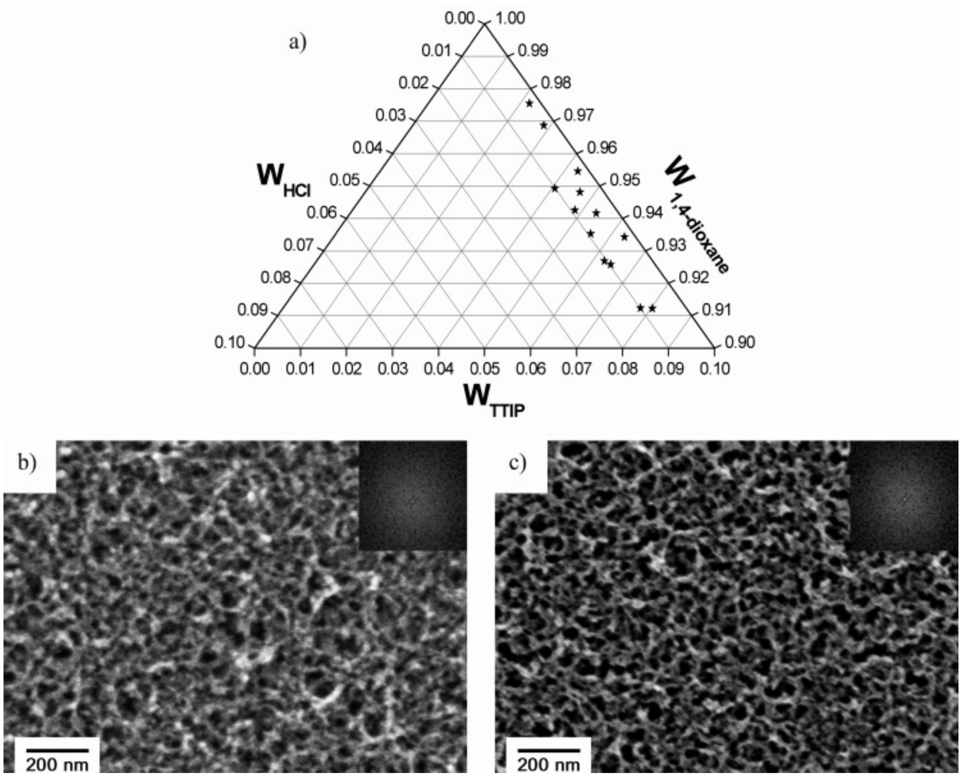

Figure 12. SEM images of TiO_2 films with foamlike structures before and after calcination. (a) Compositional existence region in the phase diagram (*W*, weight fraction). (b) SEM image before calcination. (c) SEM image after calcination. The insets in the images are FFT patterns of the corresponding structures.

With increasing weight fractions of HCl solution compared to those of the clustered nanoparticles and flakelike structures, cylinder micelles are formed (Figure 13, panels c1 and c2). The neighboring cylinder micelles can be linked to form junctions, whose number is increased with increasing amounts of TTIP, leading to the formation of mesoscale network of interconnected nanowires.

In comparison to nanowire structures, vesicles structures are formed with further increasing weight fractions of HCl (Figure 13, panels d1 and d2). Due to different ratios of vesicle size to wall thickness, different morphologies are present either directly in the dry film (nanogranulas) or after calcination (nanodoughnuts and collapsed vesicles). If the HCl fraction is roughly less than 0.03, the vesicle structures in the film can survive calcination and nanodoughnut-like structures can be obtained. If the weight fraction of HCl is increased (more than 0.04) and TTIP fraction remains unchanged, the vesicle structures collapse into disordered structures after calcination (Figure 13, panels e1 and e2). When the weight fraction of HCl is fixed relative to that of the nanodoughnuts and the amount of TTIP is increased, nanogranular structures are formed via the squashing process during spin coating.

When the surface energy between the PS block domain and the solvents outside the domain exceeds the stabilization energy limit of the micelles, a phase transition from micelles to reverse micelles happens in the solution. Consequently, wormlike aggregates, which are inverted cylinder micelle structures, are obtained. After calcination, the inner PS cores are burned away and holes are formed within the wormlike aggregates.

Role of HCl. HCl plays an important role in the templating process, which guides the formation of titanium nanostructures with a variety of morphologies. It acts not only as a catalyst for the hydrolysis of TTIP but also a retardant for the condensation. It is very important for a controlled nanostructure formation that the condensation step is retarded; otherwise the rapid and violent condensation will proceed beyond the templating boundary of the block copolymer to form unspecific large-scale structures. As a result the solution will be turbid because of the precipitation of Ti−O− species, where homogeneous films cannot be obtained via the spin-coating process.

The hydrolysis and condensation of TTIP is intrinsically a kinetic process, and the structures will evolve along with time. However, in our studies, chemicals are mixed within 3 min and further stirred for from ca. 30 min to 1 h. There is no significant structure evolution within the sample preparation time range as proved by SEM images (see the Supporting Information Figure S-3). After spin coating, it is believed that the structures within the films are frozen because there are almost no solvents remaining in the film, and the majority PS block is glassy at room temperature.

Impact of Humidity on Morphologies. It has been reported that the external humidity plays an important role on the morphology of the composite films.[34,75−83] Our samples are

---

(75) Gibaud, A.; Dourdain, S.; Gang, O.; Ocko, B. M. *Phys. Rev. B* **2004**, *70*, 161403(R).

(76) Choi, S. Y.; Mamak, M.; Coombs, N.; Chopra, N.; Ozin, G. A. *Adv. Funct. Mater.* **2004**, *14*, 335−344.

(77) Grosso, D.; Cagnol, F.; Soler-Illia, G. J. D. A. A.; Crepaldi, E. L.; Amenitsch, H.; Brunet-Bruneau, A.; Bourgeois, A.; Sanchez, C. *Adv. Funct. Mater.* **2004**, *14*, 309−322.

(78) Grosso, D.; Soler-Illia, G. J. D. A.; Crepaldi, E. L.; Cagnol, F.; Sinturel, C.; Bourgeois, A.; Brunet-Bruneau, A.; Amenitsch, H.; Albouy, P. A.; Sanchez, C. *Chem. Mater.* **2003**, *15*, 4562−4570.

(79) Soler-Illia, G. J. D. A.; Crepaldi, E. L.; Grosso, D.; Sanchez, C. *Curr. Opin. Colloid Interface Sci.* **2003**, *8*, 109−126.

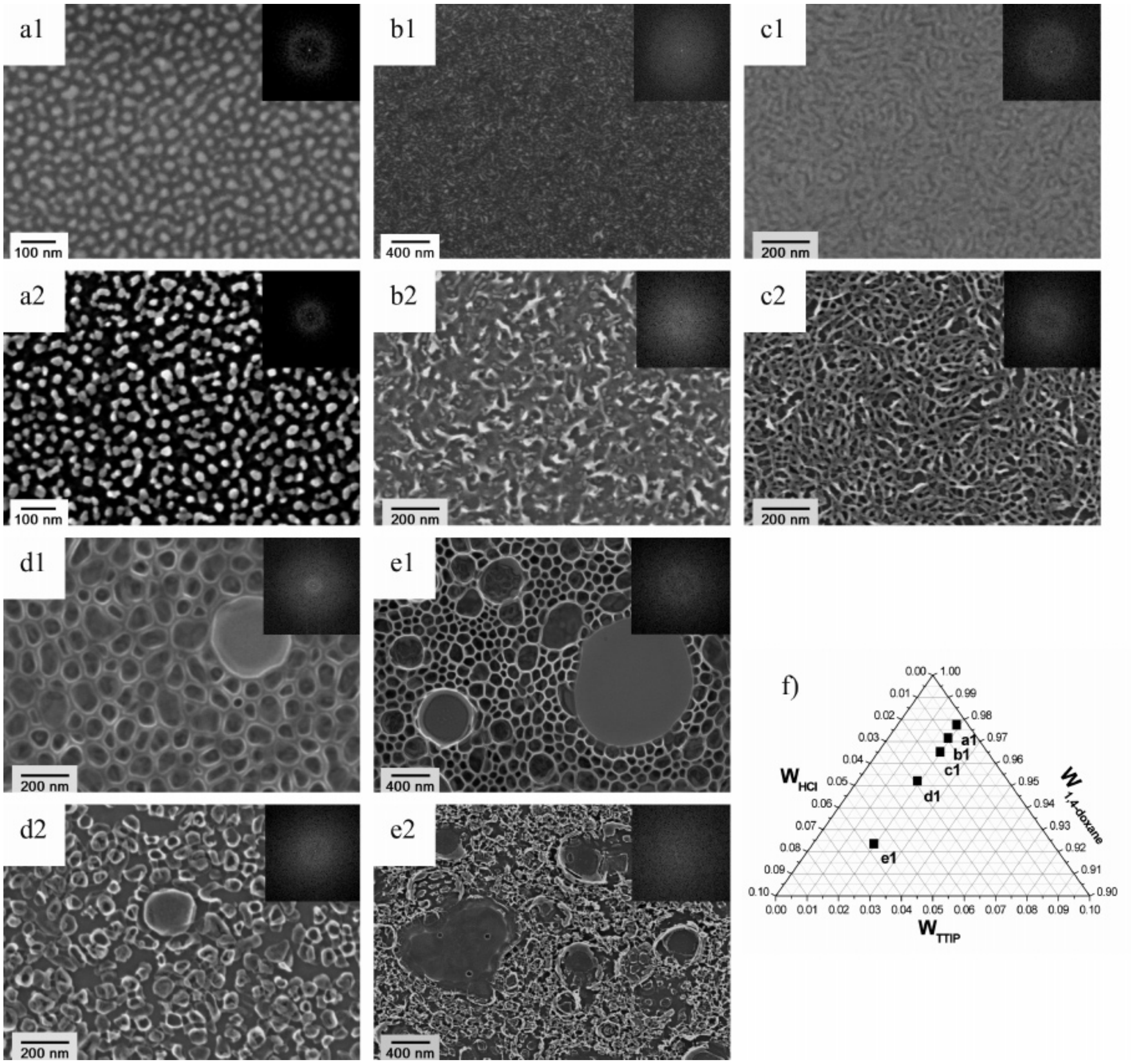

Figure 13. SEM images of TiO$_2$ films with morphology evolution with increasing HCl weight fractions. Panels a1−e1: SEM images before calcination. Panels a2−e2: SEM images after calcination. Panel f: the compositional existence regions in the phase diagram where the five structures are formed with increasing HCl weight fractions from a to e (*W*, weight fraction). The insets in the images are FFT patterns of the corresponding structures.

generally prepared in a climatized lab with a typical relative humidity of 35−45% and temperature of 21 °C. To study the humidity effects in detail, we spin coat the same stock sample solutions in ambient condition (relative humidity 41−42%) and in a glovebox, respectively (absolute humidity 0.0 ppm) (cover is open during spin coating). Figure 14 shows the corresponding morphologies of two sample series.

From the SEM images it can be seen that the morphologies are different for samples prepared under different humidity conditions. The films prepared under ambient conditions show nanowire structures of large size, and there are also a small number of vesicle structures coexisting in the film (Figure 14a1-u; film thickness, 66 nm). There is no FFT ring pattern indicating a broad size distribution of the structures. However, the sample spin coated in the glovebox is composed of small nanowire structures, and the nanowire structures are packed densely (Figure 14a2-u; film thickness, 71 nm). The clear ringlike FFT pattern (corresponding feature size, 24 nm) indicates that the spacing between nanowires is uniform. Generally, after calcination both films exhibit nanowire morphologies (Figure 14, panels a1-c and a2-c). However, the film prepared in air shows a mesoscale open framework composed of nanowires and junction points. The weak FFT ring pattern corresponds to a size of 54 nm. The sample prepared in the glovebox shows a finer nanowire network. In comparison to Figure 14a1-c, there is a clear ringlike FFT pattern, which corresponds to a spacing of 24 nm between nanowires.

For the b sample series, the size of the nanowire structures in the film prepared in the glovebox is again smaller than that prepared in air (Figure 14b2-u, film thickness, 71 nm and Figure 14b1-u, film thickness, 69 nm). Both SEM images show ringlike FFT patterns with feature sizes of 39 and 24 nm, respectively. Therefore, the nanowires in Figure 14b2-u are packed more densely than those in Figure 14b1-u. After calcination, the mesoscale network of the sample prepared in

---

(80) Crepaldi, E. L.; Soler-Illia, G. J. D. A.; Grosso, D.; Sanchez, C. *New J. Chem.* **2003**, *27*, 9−13.

(81) Crepaldi, E. L.; Soler-Illia, G. J. D. A.; Grosso, D.; Albouy, P. A.; Amenitsch, H.; Sanchez, C. *Stud. Surf. Sci. Catal.* **2002**, *141*, 235−242.

(82) Grosso, D.; Soler-Illia, G. J. D. A.; Babonneau, F.; Sanchez, C.; Albouy, P. A.; Brunet-Bruneau, A.; Balkenende, A. R. *Adv. Mater.* **2001**, *13*, 1085−1090.

(83) Sakatani, Y.; Grosso, D.; Nicole, L.; Boissiere, C.; Soler-Illia, G. J. D. A.; Sanchez, C. *J. Mater. Chem.* **2006**, *16*, 77−82.

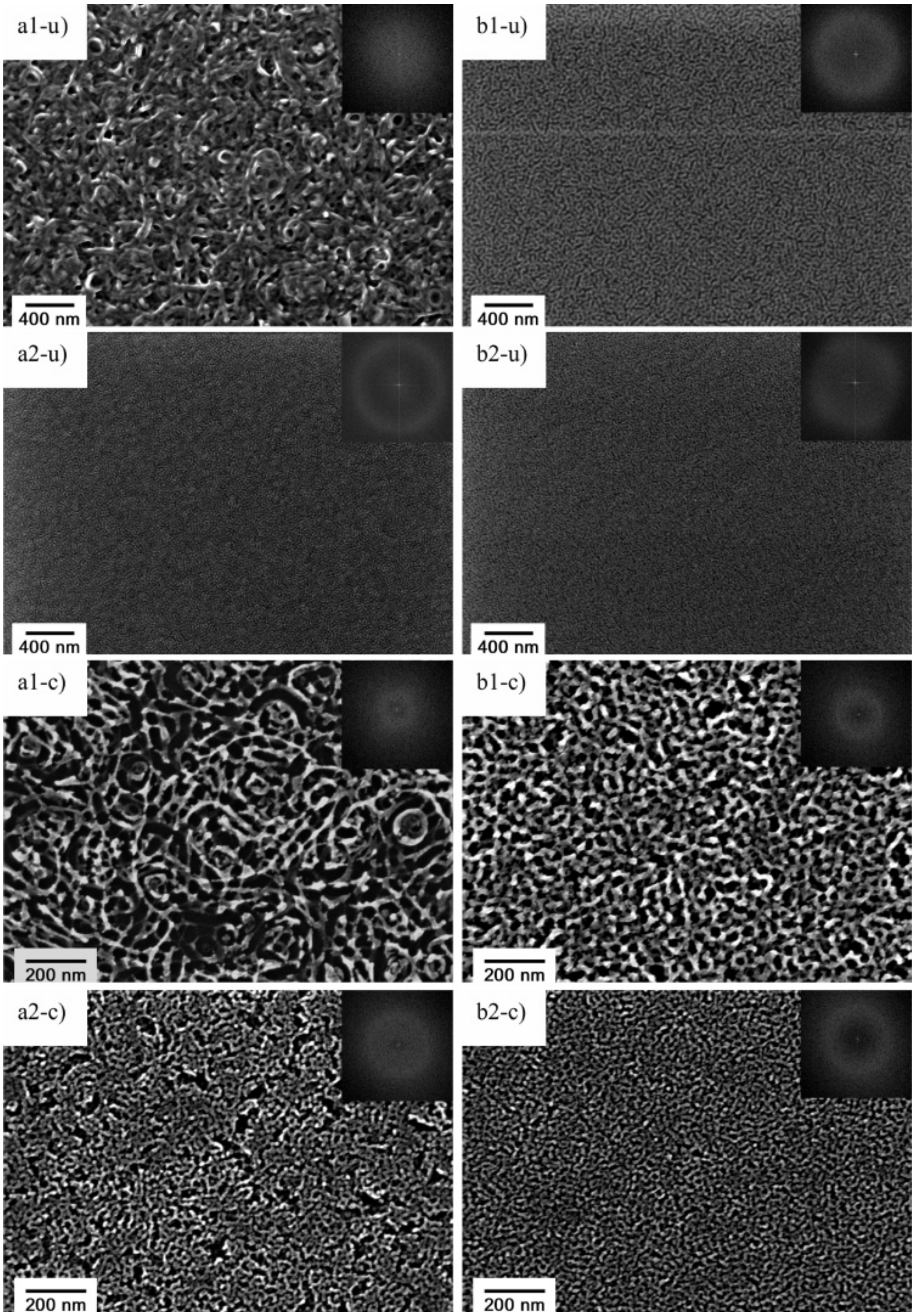

Figure 14. SEM images of samples prepared under different humidity conditions. Panels a1-u and b1-u: spin coated under ambient conditions with a relative humidity of 41−42% and temperature of 21.3 °C. Panels a2-u and b2-u: spin coated in a glovebox with an absolute humidity of 0.0 ppm and temperature of 22.0 °C. The a and b series samples were spin coated from the same stock solution, respectively. Panels a1-c and b1-c are the corresponding SEM images of samples a1-u and b1-u after calcination, respectively; panels a2-c and b2-c are the corresponding SEM images of samples a2-u and b2-u after calcination, respectively. Calcination conditions: ramp rate, 6.25 °C/min from 25 to 400 °C, 400 °C for 4 h. Composition ratios, a series: W_{TTIP}, 0.011; $W_{\mathrm{1,4\text{-}dioxane}}$, 0.972; W_{HCl}, 0.016. Composition ratios, b series: W_{TTIP}, 0.025; $W_{\mathrm{1,4\text{-}dioxane}}$, 0.971; W_{HCl}, 0.004. The insets are FFT profiles of the corresponding structures. The accelerating voltage of the SEM measurement is 3 kV for the samples after calcination.

air is more porous than the one prepared in the glovebox, which is in agreement with the structures before calcination (Figure 14, panels b1-c and b2-c). There are still ringlike FFT patterns in both images, and the feature sizes are 44 and 26 nm, respectively.

By comparing the morphologies of the two sample series spin coated in air and in the glovebox, it can be concluded that the external humidity influences the size scales of the structures present after spin coating. The external humidity in air may enhance the hydrolysis and condensation process during spin coating, and as a result, the structures formed after spin coating have a large size scale and are loosely packed. It seems that the external humidity influences sample a1 stronger than sample b1. The reason for this phenomenon can be rationalized by analyzing the role of HCl solution. The weight ratio of HCl solution in sample a1 is higher than that in sample b1, which

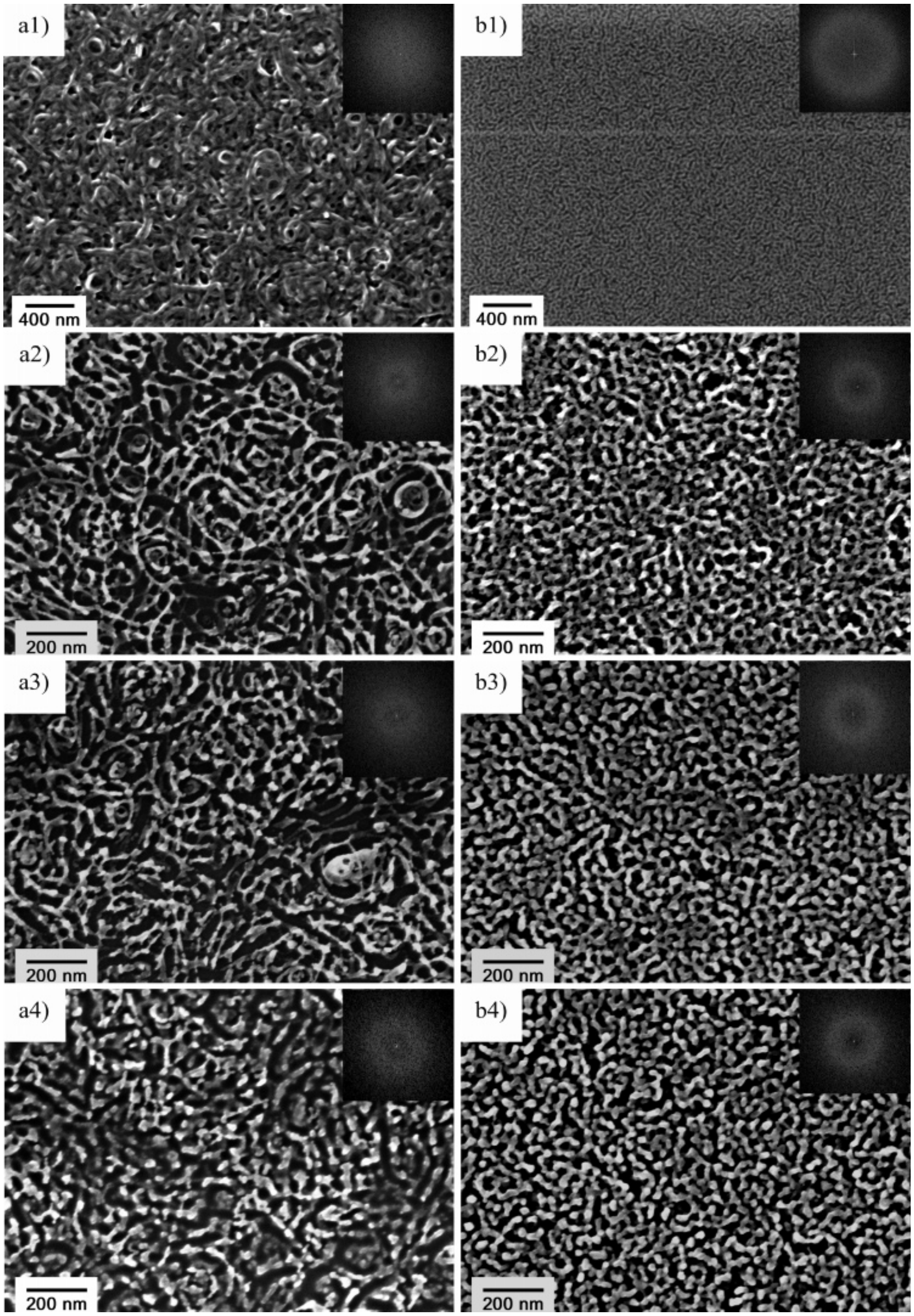

Figure 15. SEM images of films calcined at different temperatures. Panels a1 and b1: as-prepared. Panels a2 and b2: calcined at 400 °C. Panels a3 and b3: calcined at 500 °C. Panels a4 and b4: calcined at 600 °C. Ramp rate: 6.25 °C/min starting from 25 °C. Calcination time: 4 h. Composition ratios, a series: W_{TTIP}, 0.011; $W_{\mathrm{1,4\text{-}dioxane}}$, 0.972; W_{HCl}, 0.016. Composition ratios, b series: W_{TTIP}, 0.025; $W_{\mathrm{1,4\text{-}dioxane}}$, 0.971; W_{HCl}, 0.004. The insets are FFT profiles of the corresponding structures. The accelerating voltage of the SEM measurement is 3 kV for the samples after calcination.

means there is more water in sample a than in sample b. As a result, the solution is dried more slowly, and therefore the time available for internal condensation and coagulation is longer for sample a than for sample b.

Calcination Temperature Effects. It has been reported that the mesostructures may undergo structure rearrangement up to complete collapse when calcined at elevated temperatures higher than 450 °C.[50,75,80−83] To check the stability of the structures we conducted the calcination experiments at different temperatures ranging from 400 to 600 °C. Figure 15 shows the morphology evolution of two sample series with increasing calcination temperature.

For sample series a, it can be observed that all the films after calcination show nanowire structures. The morphologies in the samples calcined at 400 °C show similarities with those of as-prepared films (Figure 15, panels a2 and a1). The feature size from FFT is 54 nm. In comparison to the sample calcined at 400 °C, there is almost no structural rearrangement in the films calcined at 500 °C (Figure 15a3). The spacing size between nanowires derived from FFT is 57 nm, which is in agreement

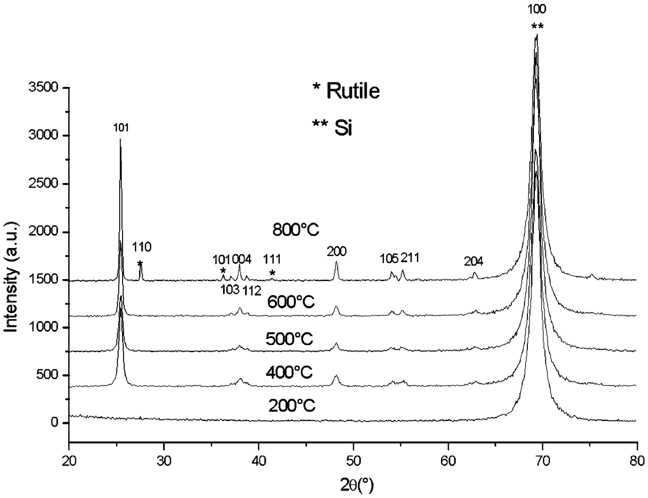

Figure 16. X-ray diffraction patterns of TiO_2 films on Si(100) substrates calcined at different temperatures for 4 h.

with the value of sample calcined at 400 °C. However, for the films calcined at 600 °C, the porous mesoscale network collapses into agglomerated nanowire structures (Figure 15a4) (FFT feature size, 55 nm).

For sample series b, the structures of films calcined at 400 °C are again in good agreement with the sample before calcination (Figure 15, panels b2 and b1) (FFT feature size, 39 nm for sample b2 and 44 nm for sample b1). There is also no significant difference between the films calcined at 400 and 500 °C (Figure 15b3) (size from FFT, 47 nm). For the films calcined at 600 °C (Figure 15b4), the connectivity between nanowires is severely destroyed, and isolated nanowire aggregates are formed (size from FFT, 47 nm).

From the comparison of the morphologies of two sample series calcined at different temperatures, it can be concluded that the films calcined at 400 °C exhibit morphologies similar to the samples before calcination. Calcination at 500 °C only induces slight nanostructure rearrangement. However, there is a severe structure rearrangement upon calcination at 600 °C, where mesoscale networks collapse into isolated nanowire agglomerates.

In comparison to the reported results,[50,75,80−83] where mesostructures were destroyed at comparable temperatures, our samples remain almost intact at temperatures up to temperatures as high as 500 °C. The relative high stability is probably because our films are ultrathin. On one hand, the absolute thermal-induced contraction normal to the substrate in an ultrathin film is smaller compared to that of thicker films. On the other hand, the substrate surface mechanically fixes the titania structures at the interface; however, in the thick films prepared by dip coating, only the structures close to the substrate surface would remain fixed, while structures further away from the interface suffer reorganization due to anisotropic stresses during calcination.

XRD Results. Figure 16 shows XRD results with different calcination temperatures (sample composition: W_{TTIP}, 0.029; $W_{1,4\text{-dioxane}}$, 0.963; W_{HCl}, 0.008). It can be seen that there is no crystallographic phase obtained after calcination at 200 °C for 4 h. Anatase phase appears when the calcination temperature increases to 400 °C. At temperatures above 800 °C, a rutile phase appears besides anatase.[15,25] From these results we conclude that the varied morphologies obtained after calcination at 400 °C for 4 h are in the anatase phase. The anatase polymorph allows using the TiO_2 films with various morphologies to possess interesting physical properties and potential applications in DSSC, which are out of the scope of this paper.

Conclusions

In this paper, PS-*b*-PEO is used as a structure-directing agent, and a good−poor solvent pair induced phase separation process is applied to produce TiO_2 films with a variety of interesting morphologies by simply adjusting the relative weight fractions between 1,4-dioxane, 37% concentrated HCl solution, and TTIP. There are micelles or reverse micelles with different morphologies formed in the solution, and the structures are further arranged via a solvent evaporation induced arrangement process during spin coating. The morphologies of the composite films before and after calcination are studied with SEM and AFM. On the basis of the results a ternary phase diagram is mapped, which can guide the preparation of nanocomposite films with desired morphologies. The formation mechanism of these morphologies is found to be comparable to that of the lyotropic phases found in block copolymer solutions. Various morphologies of pure PS-*b*-PEO are similar to those in titania−block copolymer composite films, which confirms the templating effect of the block copolymer. External humidity and calcination temperature clearly affect the resulting morphologies. However, in the humidity and temperature regimes investigated in this study, their influence is small compared to those of the changes of morphology induced by compositional changes. The XRD results prove the anatase phase in the calcined TiO_2 films. We believe that this recipe is generally applicable not only to various other types of block copolymers but also to different metal oxide sources. Thus, it opens a new simple route toward the preparation of functional metal oxide films consisting of rich novel morphologies. Further applications of these anatase TiO_2 films with different morphologies in DSSC devices are in progress and will be addressed in a separate paper.

Acknowledgment. The authors thank Gunnar Glasser for the help with FESEM, Michael Bach for the help with XRD measurements, and Prof. Dr. Werner Steffen for the help in dynamic light scattering experiments. Y. J. Cheng thanks Dr. Zaicheng Sun for his kind help at the beginning of this work. The financial support from the Max Planck Society is greatly appreciated.

Supporting Information Available: DLS curve of the solution of clustered nanoparticles, SEM image of nanowire structures with a low magnification, and SEM images of films after calcination prepared with different stirring times. This material is available free of charge via the Internet at http://pub.acs.org.

JA0562853